Supporting Information

Kinetic and Spectroscopic Response of pH-sensitive Nanoparticles: The influence of the silica-matrix

Anne Clasen,[a] Sarah Wenderoth,[b] Isabella Tavernaro,[b] Jana Fleddermann,[b] Annette Kraegeloh,[b] Gregor Jung *[a]

[a] *Biophysical Chemistry, Saarland University, Campus B2 2, 66123 Saarbrücken, Germany*

[b] *INM – Leibniz-Institute for New Materials, Campus D2 2, 66123 Saarbrücken, Germany*

Corresponding author: g.jung@mx.uni-saarland.de

1. General information

All chemicals were obtained from commercial suppliers (Sigma Aldrich, TCI, Carl Roth, Alfa Aesar, Merck or Acros Organics) and were used without further purification. All silane compounds (tetraethyl orthosilicate (TEOS) and (3-aminopropyl) triethoxysilane (APTES)), cyclohexane and L-arginine were used as received from the supplier (Sigma Aldrich) except from APTES, which was freshly distilled before use. For all syntheses and purification steps, ultrapure water was used (18.2 MΩ, Milli-Q water purification system type ELIX 20, Millipore Corp.). All NMR spectra were recorded at 25 °C on a Bruker Avance II 400 MHz nuclear magnetic resonance spectrometer (400.13 MHz (^{1}H), 100.61 MHz (^{13}C), 376.5 MHz (^{19}F)). Chemical shifts (δ) are reported in parts per million (ppm). The spectra are referenced on acetone-d_6 (δ = 2.05 ppm (^{1}H), δ = 29.84 ppm resp. δ = 206.26 ppm (^{13}C)) or $CDCl_3$ (δ = 7.26 ppm (^{1}H), δ = 77.0 ppm (^{13}C)). The multiplicities are indicated by s (singlet), d (doublet), t (triplet) and q (quartet). The associated coupling constants (*J*) are given in Hertz (Hz). The mass spectra were recorded on an AB Sciex API 5500 QTRAP with ESI as ionization method. The crystallographic data were collected on a Bruker AXS X8Apex CCD diffractometer operating with graphite-monochromatized Mo Kα radiation. Frames of 0.5° oscillation were exposed; deriving data in the θ range of 2 to 28° with a

completeness of ~98%. Structure solution and full least-squares refinement with anisotropic thermal parameters of all non-hydrogen atomes were performed using SHELX.[S1] CCDC 1904703 and 1904704 contains the supplementary crystallographic data for this paper. These data can be obtained free of charge from The Cambridge Crystallographic Data Centre via www.ccdc.cam.ac.uk/data_request/cif. A double beam Jasco V-650 spectrophotometer was used for recording absorption spectra. Fluorescence emission and excitation spectra were recorded with a Jasco FP-6500 spectrofluorometer.

2. Syntheses

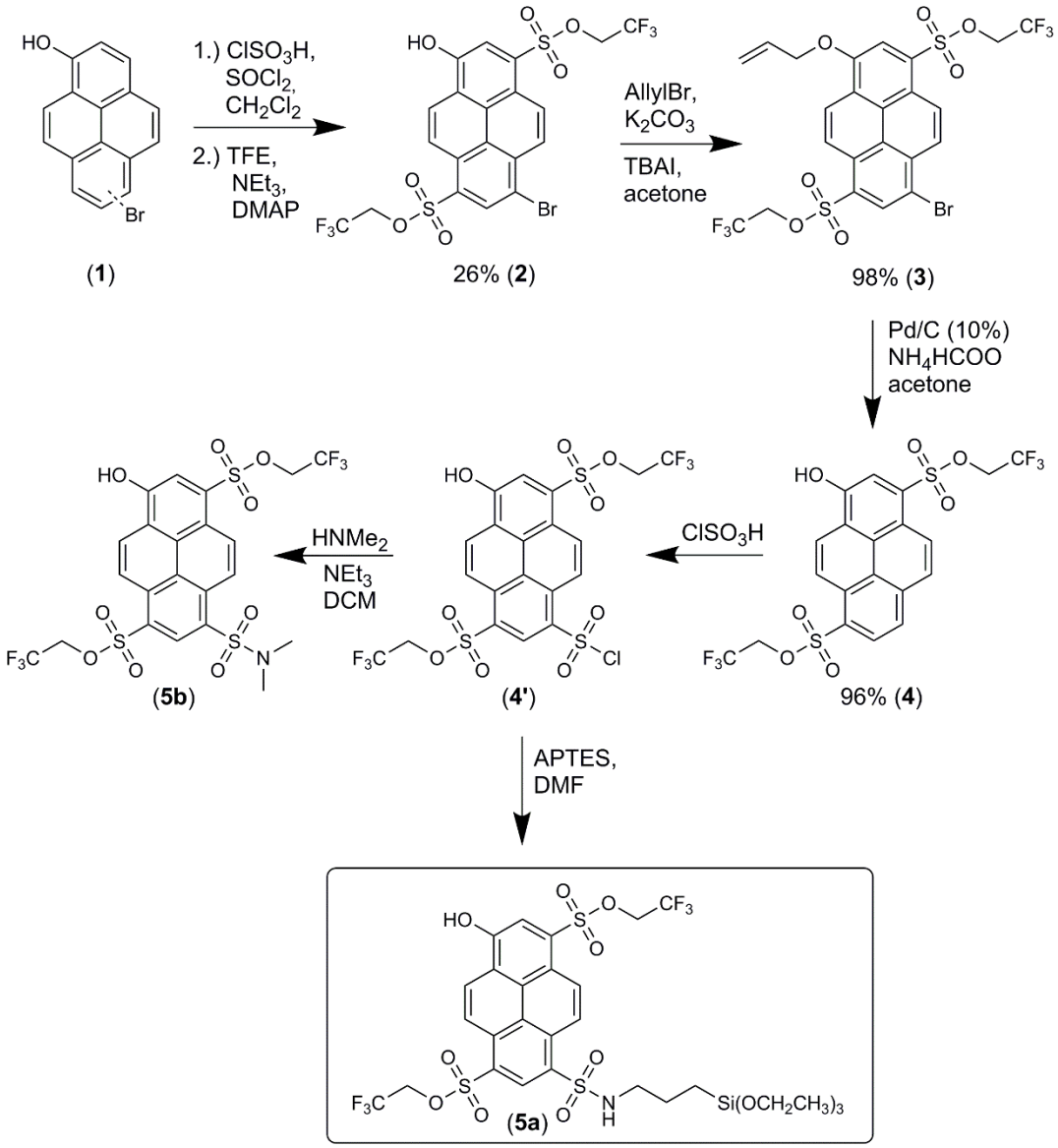

*Scheme S1: Synthesis of photoacid (**5a**) and its soluble counterpart (**5b**) for comparison.*

2.1. Bis(2,2,2-trifluoroethyl)-6-bromo-1-hydroxypyrene-3,8-disulfonate (2)

The starting material 6- and 8-bromopyren-1-ol (**1**) was synthesized analogously to previous preparations.[S2] A mixture of 6- and 8-bromopyren-1-ol (250 mg, 0.84 mmol) was dissolved in dry methylene chloride (40 mL) and cooled down to -5 °C. Chlorosulfonic acid (875.0 mg, 8.41 mmol) was added slowly and the resultant mixture was stirred for 6 hours, warming up to room temperature. Thionyl chloride was added in two portions (2x 500.2 mg, 8.42 mmol), with the second addition after 16 hours. Thereafter, the dark violet slurry was heated to reflux for 4 hours. The solvent and thionyl chloride was removed in vacuo from the reaction mixture after cooling. The residue was dissolved in dry methylene chloride (5 mL) under nitrogen and cooled to - 5 °C. Triethylamine (0.85 mg, 8.41 mmol) was added before a mixture of 2,2,2-trifluoroethanol (1.71 mg, 16.82 mmol) and 4-dimethylaminopyridine (1.74 g, 8.41 mmol). The reaction mixture was stirred for 18 hours at room temperature and the solvent was again removed in vacuo. After dissolution in ethyl acetate, the organic phase was washed three times with diluted hydrochloric acid (1 M), distilled water and saturated NaCl solution. The organic phase was dried over anhydrous sodium sulfate before the solvent was evaporated. The crude product was purified by column chromatography (eluent: ethyl acetate/petrolether 40-65 = 4:6) to yield the isolated isomer **2** (137.7 mg, 0.22 mmol, 26%) and an isomer mixture (207.2 mg, 0.33 mmol, 40%) as a yellow powder. ^{1}H-NMR (400.13 MHz, acetone-d_6, 25°C) (figure S35-S37): δ (ppm) = 11.03 (s, -OH), 9.05 (d, ^{3}J (H,H) = 9.54 Hz, Ar-H), 8.96 (s, Ar-H), 8.93 (d, ^{3}J (H,H) = 9.54 Hz, Ar-H), 8.88 (d, ^{3}J (H,H) = 9.79 Hz, Ar-H), 8.60 (d, ^{3}J (H,H) = 9.79 Hz, Ar-H), 8.50 (s, Ar-H), 4.86 (q, ^{3}J (H,H) = 8.28 Hz, CH_2-CF_3), 4.82 (q, ^{3}J (H,H) = 8.28 Hz, CH_2-CF_3). ^{13}C-NMR (100.61 MHz, acetone-d_6, 25°C) (figure S38-S40): δ (ppm) = 154.5, 134.8, 133.6, 131.4, 129.9, 128.9, 128.4, 126.5, 126.2, 126.1, 125.6, 125.3, 123.4, 122.0, 120.0, 117.5, 66.4 (q, ^{2}J (C,F) = 16.9 Hz, 3x CH_2-CF_3). ^{19}F-NMR (376.5 MHz, acetone-d_6, 25°C) (figure S41): δ (ppm) = -74.52, -74.54. MS (ESI) (figure S42): *m/z* calc. for $C_{20}H_{10}BrF_6O_7S_2^-$: 618.9 $[M\text{-}H^+]^-$, found: 618.9.

2.2. 1-(allyloxypyrene)-bis(2,2,2-trifluoroethyl)-6-bromo-3,8-disulfonate (3)

Compound **2** (87.1 mg, 0.14 mmol) was dissolved in dry acetone (5 mL), before potassium carbonate (119.2 mg, 0.86 mmol), TBAI (27.1 mg, 0.08 mmol) and allyl bromide (68.6 mg, 0.56 mmol) were added. The dark yellow reaction mixture was stirred for 5 days at room temperature. The solvent was removed in vacuo and the residue was dissolved in methylene chloride. The solution was extracted three times with diluted hydrochloric acid (1 M) and distilled water as well as with saturated NaCl, before the organic phase was dried over anhydrous sodium sulfate. After the solution was evaporated under reduced pressure, column chromatography (eluent: methylene chloride/petrol. ether 40-65 = 7:3) was used to purify the residue and yielded **3** as yellow powder (90.7 mg, 0.14 mmol, 98%). ^{1}H-NMR (400.13 MHz, $CDCl_3$, 25°C) (figure S43-S45): δ (ppm) = 9.06 (d, ^{3}J (H,H) = 9.54 Hz, Ar-H), 9.00 (s, Ar-H), 8.99 (d, ^{3}J (H,H) = 10.29 Hz, Ar-H), 8.89 (d, ^{3}J (H,H) = 9.54 Hz, Ar-H), 8.61 (d, ^{3}J (H,H) = 9.79 Hz, Ar-H), 8.32 (s, Ar-H), 6.26 (ddt, ^{3}J (H,H) = 17.32 Hz, ^{3}J (H,H) = 10.54 Hz, ^{3}J (H,H) = 5.27 Hz, CH), 5.65 (dd, ^{3}J (H,H) = 17.32 Hz, ^{3}J (H,H) = 1.25 Hz, CH), 5.51 (dd, ^{3}J (H,H) = 10.54 Hz, ^{3}J (H,H) = 1.25 Hz, CH), 5.06 (dt, ^{3}J (H,H) = 5.27 Hz, ^{3}J (H,H) = 1.25 Hz, CH), 4.46 (q, ^{3}J (H,H) = 7.78 Hz, CH_2-CF_3), 4.45 (q, ^{3}J (H,H) = 7.78 Hz, CH_2-CF_3). ^{13}C-NMR (100.61 MHz, $CDCl_3$, 25°C) (figure S46-S48): δ (ppm) = 153.4, 134.2, 132.6, 131.5, 129.8, 128.7, 127.9, 126.7, 125.8, 125.7, 125.4, 125.2, 124.5, 123.0, 122.5, 121.6 (q, ^{1}J (C,F) = 274.3 Hz, 2x C, 2 CF_3), 120.3, 120.2, 119.5, 112.0, 70.5, 65.1 (q, ^{2}J (C,F) = 38.9 Hz, 3x CH_2-CF_3). ^{19}F-NMR (376.5 MHz, $CDCl_3$, 25°C) (figure S49): δ (ppm) = -73.60, -73.61.

2.3. Bis(2,2,2-trifluoroethyl)-1-hydroxypyrene-3,8-disulfonate (4)

Ammonium formate (385.9 mg, 6.12 mmol) and palladium on carbon (10 wt%, 132 mg) were added to a solution of **3** (87.1 mg, 0.13 mmol) in dry acetone (40 mL) and the reaction was heated to reflux. After the fluorescence has changed from blue to yellow-green, the mixture was stirred for another hour. The reaction mixture was cooled to room temperature, before the suspension was filtered through celite. The solvent of the resulting solution was evaporated under reduced pressure. Afterwards the residue was dissolved in ethyl acetate and washed three times with diluted

hydrochloric acid (1 M), distilled water and saturated NaCl. The organic phase was dried over anhydrous sodium sulfate and evaporated under reduced pressure. **4** (68.6 mg, 0.13 mmol, 96 %) was obtained as yellow powder. ^{1}H-NMR (400.13 MHz, acetone-d_6, 25°C) (figure S50-S52): δ (ppm) = 9.00 (d, ^{3}J (H,H) = 9.54 Hz, Ar-H), 8.92 (d, ^{3}J (H,H) = 9.54 Hz, Ar-H), 8.87 (d, ^{3}J (H,H) = 9.54 Hz, Ar-H), 8.80 (d, ^{3}J (H,H) = 8.28 Hz, Ar-H), 8.57 (d, ^{3}J (H,H) = 8.28 Hz, Ar-H), 8.46 (s, Ar-H), 8.40 (d, ^{3}J (H,H) = 9.54 Hz, Ar-H), 4.80 (q, ^{3}J (H,H) = 8.2 Hz, CH_2-CF_3), 4.78 (q, ^{3}J (H,H) = 8.2 Hz, CH_2-CF_3). ^{13}C-NMR (100.61 MHz, acetone-d_6, 25°C) (figure S53-S56): δ (ppm) = 153.9, 136.7, 130.5, 130.5, 128.2, 128.0, 127.3, 126.8, 126.6, 125.7, 125.3, 124.89, 124.85, 123.54, 122.46, 122.14, 122.09, 116.6, 66.2 (q, ^{2}J (C,F) = 16.9 Hz, 3x CH_2-CF_3). ^{19}F-NMR (376.5 MHz, acetone-d_6, 25°C) (figure S57): δ (ppm) = -74.52, -74.53. MS (ESI) (figure S58): *m/z* calc. for $C_{20}H_{11}F_6O_7S_2^-$: 540.99 $[M\text{-}H^+]^-$, found: 540.9.

2.4. Bis(2,2,2-trifluoroethyl)-1-hydroxypyrene-6-(*N*-(3-(triethoxysilyl)propyl)sulfamoyl)-3,8-disulfonate (5a) and Bis(2,2,2-trifluoroethyl)-1-hydroxypyrene-6-(*N,N*-dimethylsulf-amoyl)-3,8-disulfonate (5b)

Compound **4** (20 mg, 36.8 µmol) was dissolved in chlorosulfonic acid (5.25 g, 45.1 mmol) at -10 °C. After stirring for 3 hours at 60 °C, the black mixture was slowly dropped to crushed ice and the aqueous solution was extracted three times with ethyl acetate. The combined organic solutions were washed with saturated NaCl and dried over anhydrous sodium sulfate. After evaporation under reduced pressure, **4'** was obtained which was not characterized further. The residue (2.24 mg, 3.49 µmol) was then dissolved in DMF (995 µL) and triethylamine (181 µg, 1.75 µmol) as well as APTES (2.36 mg, 10.5 µmol) were added to yield **5a**. The compound **5a** was used without yield determination. Compound **5b** was prepared in an analogous manner from **4'** and dimethylamine. MS (ESI) (figure S59): *m/z* calc. for $C_{22}H_{16}F_6NO_9S_3^-$: 648.00 $[M\text{-}H^+]^-$, found: 648.0.

2.5. Syntheses and purification of modified core nanoparticles [S3]

In a three-neck round bottom flask, 91 mg (0.52 mmol) L-arginine was dissolved in 69 mL of water or deuterium oxide and 4.5 mL of cyclohexane was added. The biphasic water/cyclohexane system was heated to 40 °C under stirring. Hereafter 5.5 mL (24.63 mmol) of TEOS was added to the top layer. To synthesize unstained nanoparticles, the emulsion was stirred for 20 hours at 150 rpm.

For obtaining labelled nanoparticles the emulsion was stirred for 30 min after addition of TEOS. Afterwards 500 µL of dye **5a** in DMF (3.49 mmol μL^{-1}) were injected to the aqueous phase and the mixture was kept under these conditions for further 20 h. Finally, the obtained nanoparticles were purified by dialysis (Nadir-dialysis tubing MWCO 10 kDa, Carl Roth) against 4 L Milli-Q water for 4 h. The water was exchanged after 30, 90 and 180 min. Finally, the silica nanoparticles were filtered by using 0.22 µm cellulose acetate membrane filters (Carl Roth).

2.6. Cladding by an unstained silica layer providing core-shell nanoparticles

14 mg (0.08 mmol) L-arginine was dissolved in 36 mL of water or deuterium oxide. This solution was combined with 10 mL core nanoparticles (see previous section) and 5 mL of cyclohexane. After the biphasic system was heated to 40 °C, 3.52 mL of TEOS was added and the mixture was stirred for further 20 h. The purification took place as described above.

2.7. Cladding by a stained silica layer providing core-shell nanoparticles

14 mg (0.08 mmol) of L-arginine was dissolved in 36 mL of water or deuterium oxide. This solution was combined with 10 ml core nanoparticles (see previous section) and 5 mL of cyclohexane. After the biphasic system was heated to 40 °C, 3.52 mL of TEOS was added. After 30 min, 500 µL of dye **5a** in DMF (3.49 mmol μL^{-1}) were injected to the aqueous phase and the mixture was stirred further 20 h. The purification took place as described above.

3. Transmission Electron Microscopy (TEM)

Morphology and mean particle diameter were determined using a JEM-2100F microscope (JEOL), taken with a LaB6 cathode, a HR-pol, a condenser aperture and a high contrast aperture. An acceleration voltage of 200 kW and an Orius SC1000 camera (Gatan) was used. The particle size distribution was determined on a random sample of 50 nanoparticles using the XImageJ software (Version: 1.45 s, winPenPack X-ImageJ Launcher from the National Institute of Health (http:// rsb.info.nih.gov/ij/) (table S1). TEM images are presented in figure S1 and S2.

Table S1: Diameter of core and core-shell nanoparticles by TEM

	d_{TEM}(C-NP) [nm]	dispersity of C-NP [%]	d_{TEM}(CS-NP) [nm]	dispersity of CS-NP [%]
unlabelled	16.5 ± 1.4	8.6	24.7 ± 2.4	9.6
labelled	23.7 ± 2.3	9.6	32.6 ± 2.3	7.2
labelled in D_2O	28.2 ± 2.6	9.4	32.2 ± 3.1	9.7

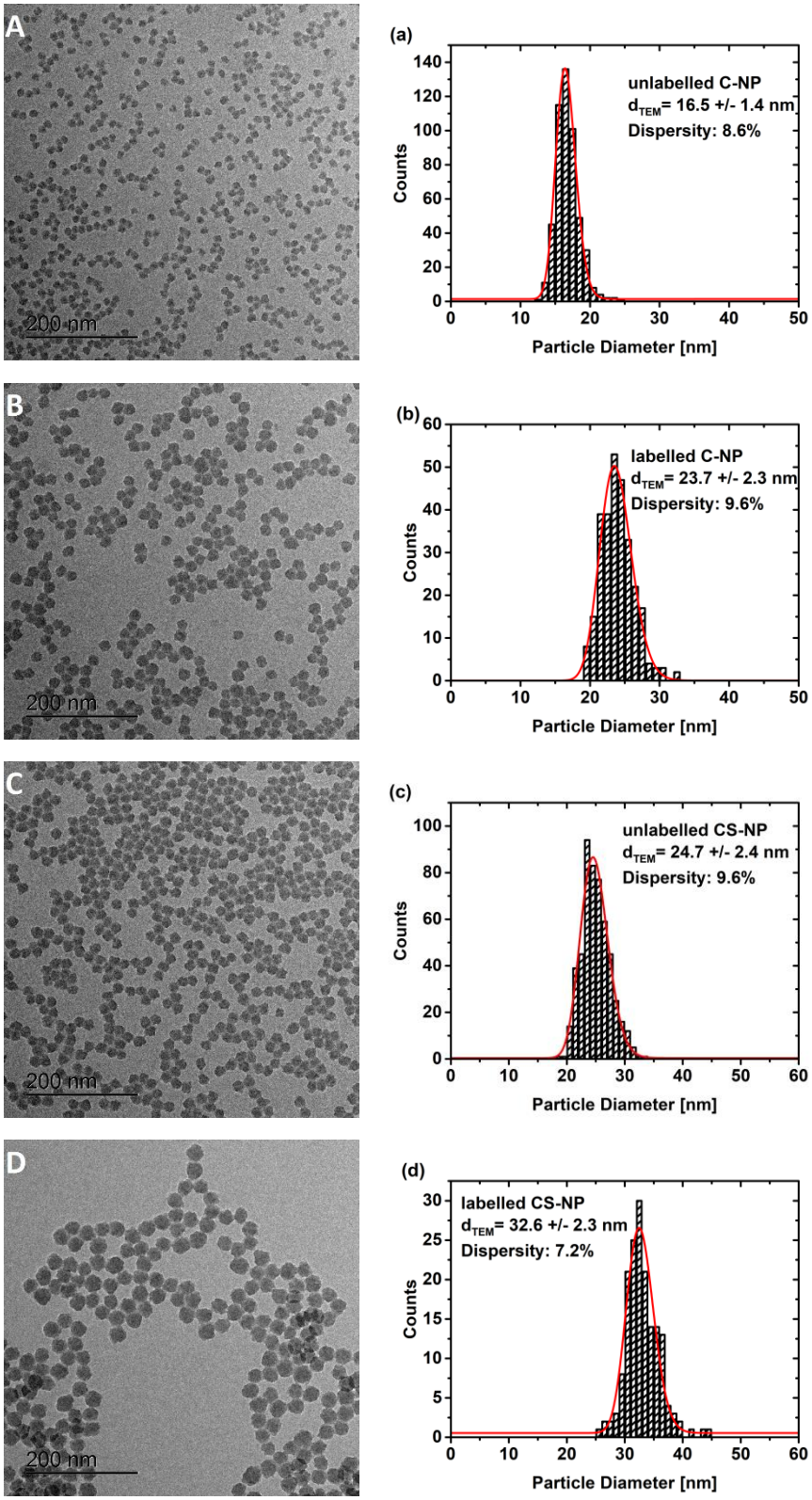

Figure S1: TEM images and histogram of unlabelled core nanoparticles (a, d_{TEM}= 16.5 ± 1.4 nm), labelled core nanoparticles (b, d_{TEM}= 23.7 ± 2 .3 nm), unlabelled core-shell nanoparticles (c, d_{TEM}= 24.7 ± 2.4 nm), and embedded dye core-shell nanoparticles (d, d_{TEM}= 32.6 ± 2.3 nm).

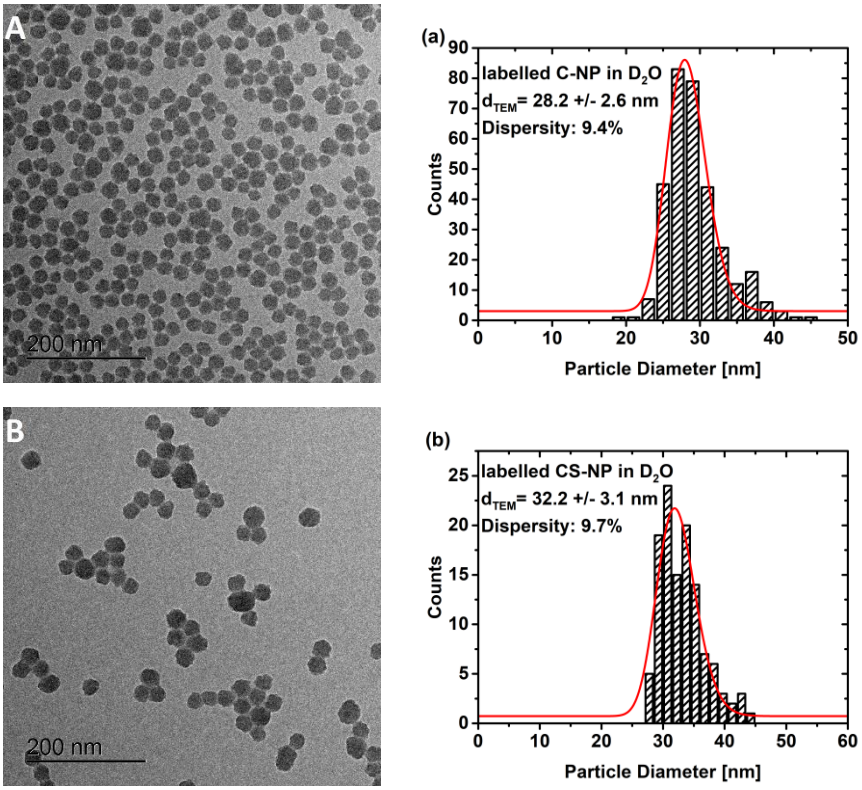

Figure S2: TEM images and histogram of labelled core nanoparticles in D_2O (a, d_{TEM}= 28.2 ± 2.6 nm) and labelled core-shell nanoparticles in D_2O (b, d_{TEM}= 32.2 ± 3.1 nm).

4. Dynamic Light Scattering (DLS)

The hydrodynamic diameter (d_h) of core nanoparticles (C-NP) and core-shell nanoparticles (CS-NP) was determined by DLS measurements using a Zetasizer Nano ZSP (Malvern Instruments). All measurements were performed in triplicate. The samples were diluted 1:10 in Milli-Q water or D_2O. The suspensions were analysed in disposal cuvettes, the temperatue was set to 25 °C and the suspension viscosity (0.887 cP) and refractive index (1.330) were assumed to be that of ultrapure water, corrected for temperature. A calculated value of 1.420 was used for the refractive index of the silica nanoparticles. Each measurement data was obtained by three runs with several subruns (10 seconds per subrun). Samples were irradiated with a laser (HeNe laser; λ= 633 nm) and the intensity fluctuation of the scattered light, detected at a backscattering angle of 173°, was analysed in automatic mode to obtain the autocorrelation function. The mean hydrodynamic diameter d_h was determined by a size distribution using a regularization scheme by intensity (figure S3 and S4). For comparison of the

results z-average, the intensity based harmonic mean, and the polydispersity index (PDI), an indication of the width of the overall distribution, are given in table S2.

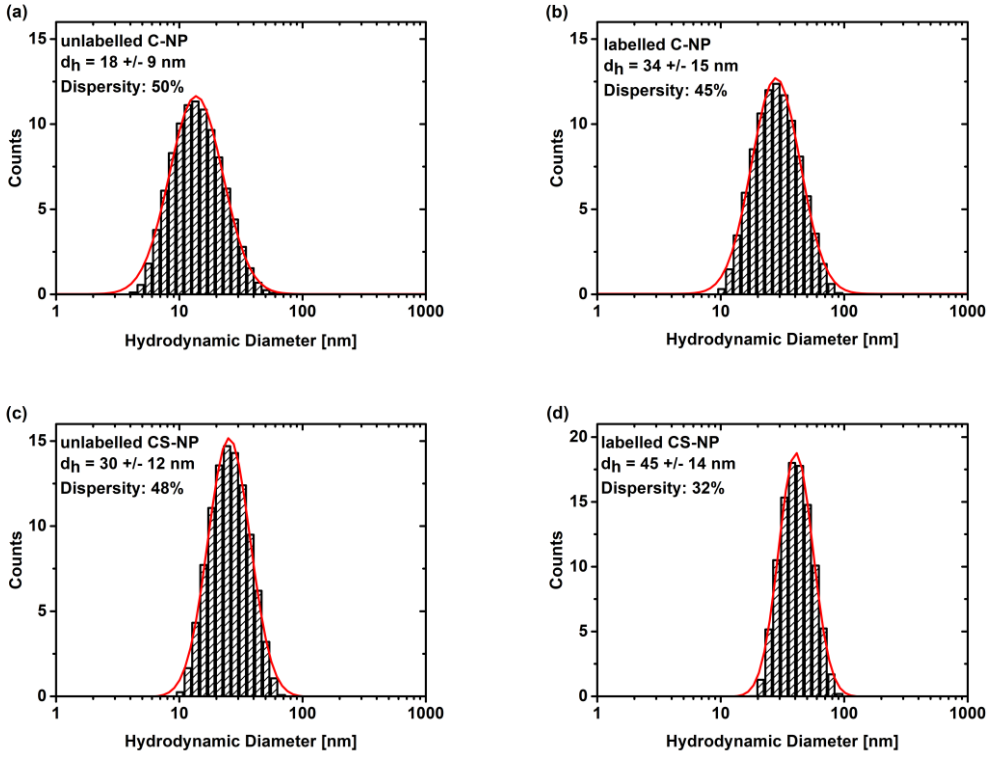

Figure S3: DLS analysis of unlabelled core nanoparticles (a, d_h= 18 ± 9 nm), labelled core nanoparticles (b, d_h= 34 ± 15 nm), unlabelled core-shell nanoparticles (c, d_h= 30 ± 12 nm), and embedded dye core-shell nanoparticles (d, d_h= 45 ± 14 nm). The mean hydrodynamic diameter (d_h) is expressed as the lognormal distribution for the intensity density and the dispersity (p) is calculated with the formula $= {}^{\sigma}/_{\mu}$ *; σ = standard deviation, μ = mean value.*

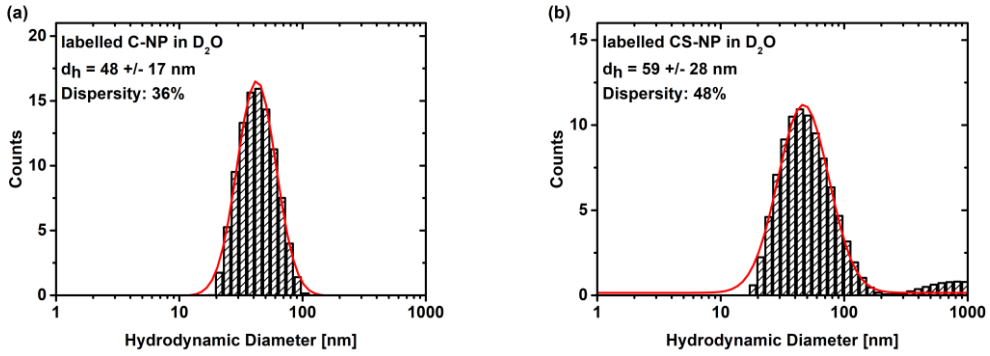

Figure S4: DLS analysis of labelled core nanoparticles in D_2O (a, d_h= 48 ± 17 nm) and labelled core-shell nanoparticles in D_2O (b, d_h= 59 ± 28 nm). The mean hydrodynamic diameter (d_h) is expressed as the lognormal distribution for the intensity density and the dispersity (p) is calculated with the formula $= {}^{\sigma}/_{\mu}$ *; σ = standard deviation, μ = mean value.*

Table S2: z-average and polydispersity index (PDI) of core and core-shell nanoparticles by DLS

	z-average (C-NP) [nm]	PDI of C-NP [%]	z-average (CS-NP) [nm]	PDI of CS-NP [%]
unlabelled	13	21	24	12
labelled	28	21	40	7
labelled in D_2O	40	9	50	25

5. ζ-potential

The ζ-potential was recorded using a Zetasizer Nano ZSP (Malvern Instruments) and the samples were diluted in 10 mM KCl (9:1). The ζ-potential of all nanoparticles was calculated using their electrophoretic mobility (figure S5).

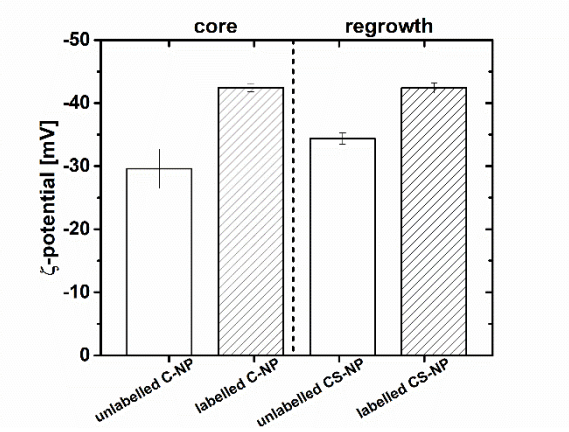

Figure S5: ζ-potential of unlabelled and labelled core and core-shell nanoparticles.

6. Fluorescence excitation and emission spectra

Fluorescence excitation and emission spectra of **5a** (figure S6, table S3), core nanoparticles (C-NP) (figure S7a, table S3) and core-shell nanoparticles (CS-NP) (figure S7b, table S3) were recorded in commercial buffer (20 mM HPCE-buffer, sodium citrate and sodium phosphate, Fluka/Honeywell).

*Table S3: Maxima of excitation and emission spectra of **5a**, C-NP and CS-NP*

	ROH			RO^-		
	5a	**C-NP**	**CS-NP**	**5a**	**C-NP**	**CS-NP**
$\lambda_{ex,max}$	417 nm	418 nm	416 nm	495 nm	492 nm	493 nm
$\lambda_{em,max}$	535 nm	538 nm	535 nm	545 nm	540 nm	536 nm

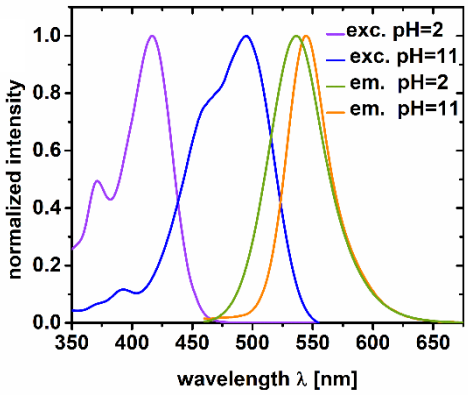

*Figure S6: Excitation (exc.) (λ_{em}= 565 nm) and emission spectra (em.) (λ_{ex}= 450 nm) of **5a** at pH 2 (ROH) and 11 (RO^-).*

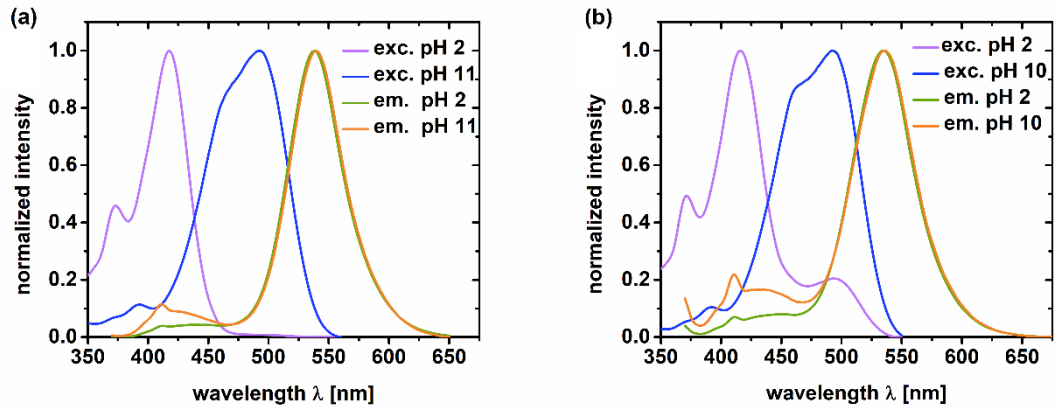

Figure S7: Excitation (exc.) (λ_{em}= 570 nm) and emission spectra (em.) (λ_{ex}= 360 nm) of C-NP (a) and CS-NP (b) at pH 2 (ROH) and 11 resp. 10 (RO^-).

7. Absorption titration

Commercial buffers (20 mM HPCE-buffer, sodium citrate and sodium phosphate) were used between pH 2 and 11. A small aliquot of a stock solution of **5a** in DMSO (figure S8a) and core nanoparticles (C-NP) in water (figure S9a), respectively, was added. Due to scattering it was not possible to obtain absorption spectra with core-shell nanoparticles (CS-NP). The fluorescence intensity *I* at λ_{max} of the photoacid (ROH) and its conjugate base (anionic, deprotonated form; RO^-) were taken at each pH from the raw spectra to calculate the molar fraction ratio *R* for each species separately [equation (S1)].[S4] I_{min} is the minimum intensity obtained in the titration and I_{max} is the maximum intensity.

$$R = \frac{I - I_{min}}{I_{max} - I_{min}} \qquad \text{(S1)}$$

The *R* values obtained via equation (S1) were plotted against the pH value, from which pK_a-values were obtained according to equation (S2) and equation (S3) (figure S8-S12). The molar fraction ratio curves intersect at their inflection point at *R* = 0.5 and give the corresponding pK_a value.

$$R(ROH) = \frac{1}{1+10^{pH-pK_a}} \qquad \text{(S2)}$$

$$R(RO^-) = 1 - \frac{1}{1+10^{pH-pK_a}} \qquad \text{(S3)}$$

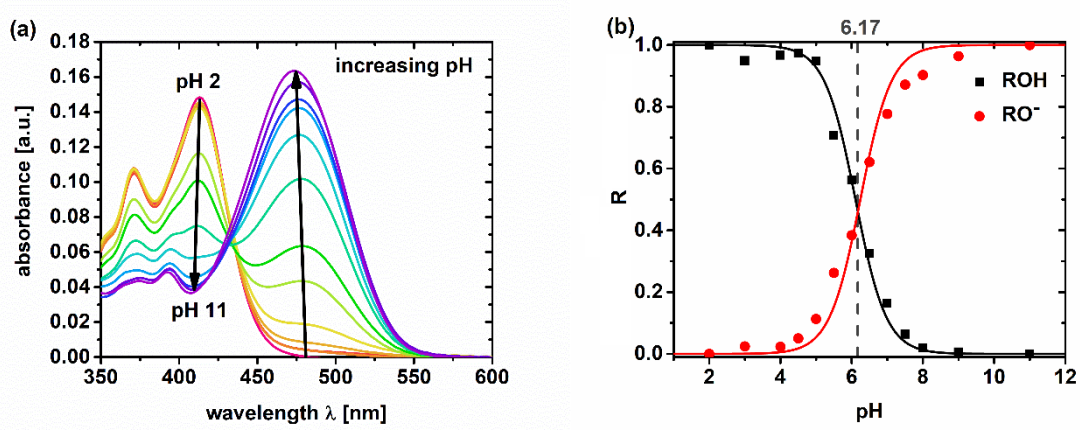

*Figure S8: Absorption titration spectra of **5a** at various pH-values (a) and the resulting titration curve (b) of ROH and RO^-.*

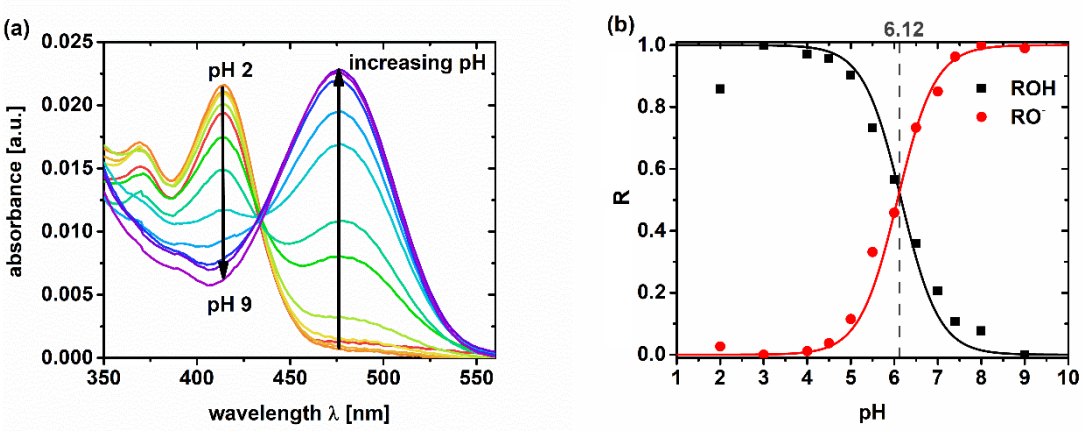

Figure S9: Absorption titration spectra of C-NP at various pH-values (a) and the resulting titration curve (b) of ROH and RO^-.

8. Fluorescence titration

Commercial buffers (20 mM HPCE-buffer, sodium citrate and sodium phosphate) were used between pH 2 and 11. A small aliquot of a stock solution of **5a** in DMSO (figure S10a) and core nanoparticles (C-NP) (figure S11a and S13a) and core-shell nanoparticles (CS-NP) in water (figure S12a and S13b), respectively, was added.

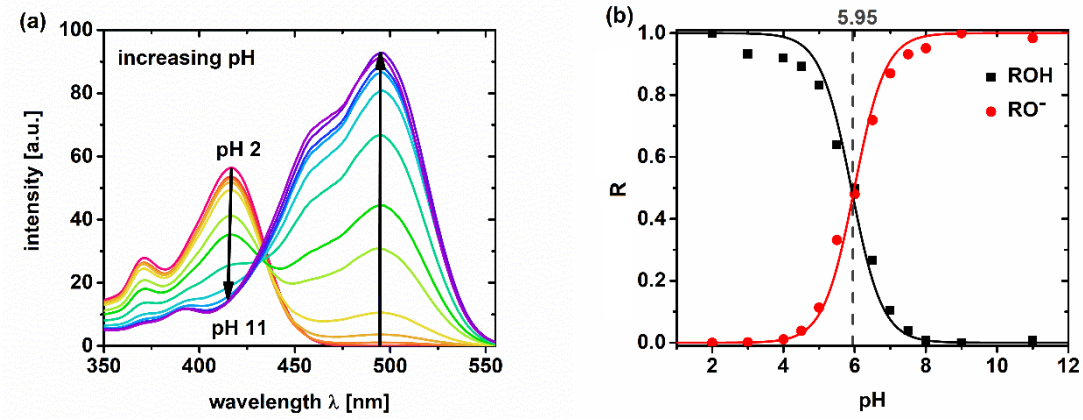

*Figure S10: Excitation titration spectra (λ_{em}= 565 nm) of **5a** at various pH-values (a) and the resulting titration curve (b) of ROH and RO^-.*

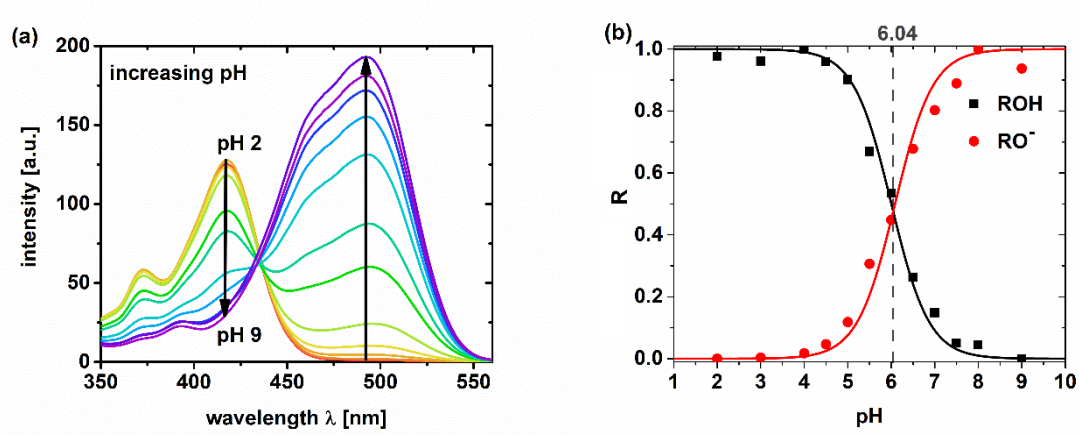

Figure S11: Excitation titration spectra (λ_{em}= 570 nm) of C-NP at various pH-values (a) and the resulting titration curve (b) of ROH and RO^-.

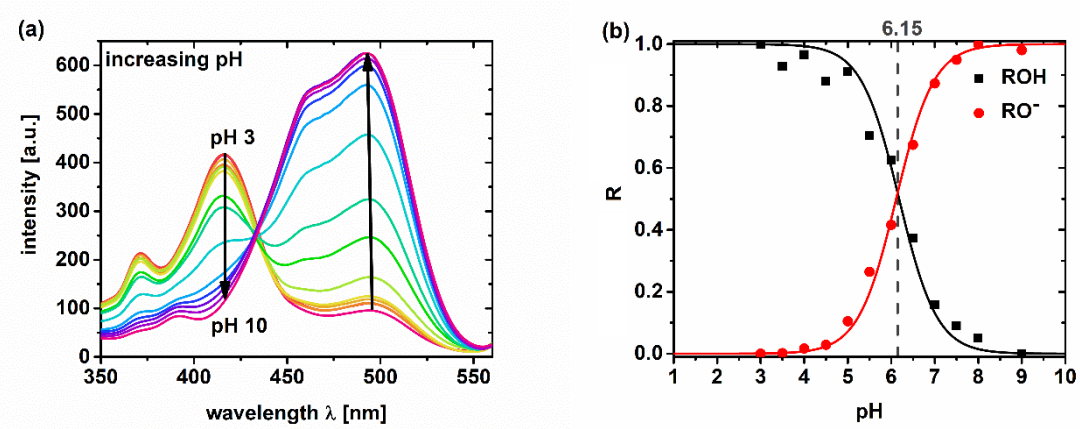

Figure S12: Excitation titration spectra (λ_{em}= 570 nm) of CS-NP at various pH-values (a) and the resulting titration curve (b) of ROH and RO^-.

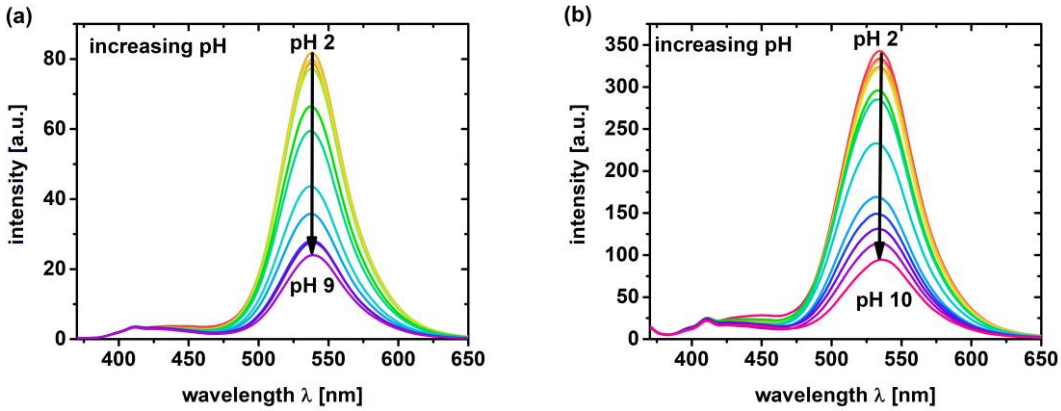

Figure S13: Emission titration spectra (λ_{ex}= 360 nm) of C-NP (a) and CS-NP at various pH-values (b).

*Table S4: pK_a-value of unbound dye **5a**, C-NP and CS-NP via absorption and fluorescence excitation titration*

	pK_a (5a)	pK_a (C-NP)	pK_a (CS-NP)
absorption titration	6.17	6.12	-
fluorescence excitation titration	5.95	6.04	6.15
mean	6.06 ± 0.11	6.08 ± 0.04	6.15

9. Steady-state fluorescence anisotropy measurements

Steady-state anisotropy was determined with the same fluorescence spectrometer as before (Jasco spectrofluorometer FP 6500) using vertical polarization for excitation and both vertical and horizontal polarization for detection. Depicted spectra were corrected for the grating factor *G* (figure S14).[S5]

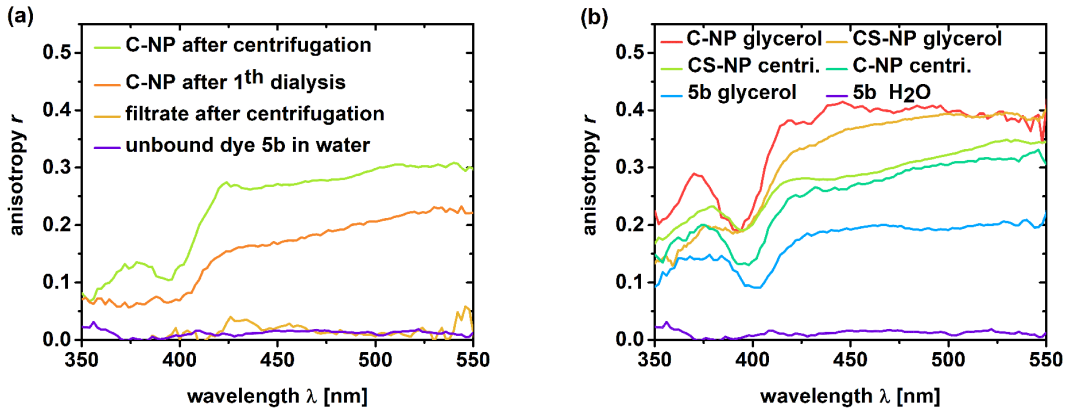

*Figure S14: Steady-state fluorescence anisotropy measurements of C-NP in water (a) and **5b**, C-NP and CS-NP in water and after addition of glycerol (b).*

10. Time-correlated single-photon counting

Accordingly, TCSPC measurements were performed with a home-build setup. Excitation was done with a fiber laser (FemtoFiber pro NIR, TOPTICA, λ= 780 nm, pulse width ~100 fs), in combination with a BBO-crystal (Laser Components) to generate λ= 390 nm, or a pulsed laser diode (PicoQuant, LDH-P-C-470, λ= 470 nm; pulse width < 100 ps), which was controlled by a diode laser driver unit (PDL 808 MC SEPIA, PicoQuant). After filtering through a band pass filter (HQ 525/50, AHF Analysentechnik), a single-photon avalanche detector (PDM 100ct SPAD, Micro Photon Devices) in combination with a photon counting device (PicoHarp 300, PicoQuant) was used for detection. The instrumental response function (IRF) was determined from the scattering of a diluted colloidal silica solution (LUDOX TM-50, Sigma Aldrich) (λ_{em}= 470 nm, IRF~300 ps (FWHM)) or an aqueous solution of erythrosine B (quenched with KI) (λ_{em}= 500-550 nm, IRF~75 ps (FWHM)). All fluorescence lifetimes were measured under magic angle conditions, except figure S16 (supporting information). The collected data was analysed using exponential fit functions (SymPhoTime, (PicoQuant) software).

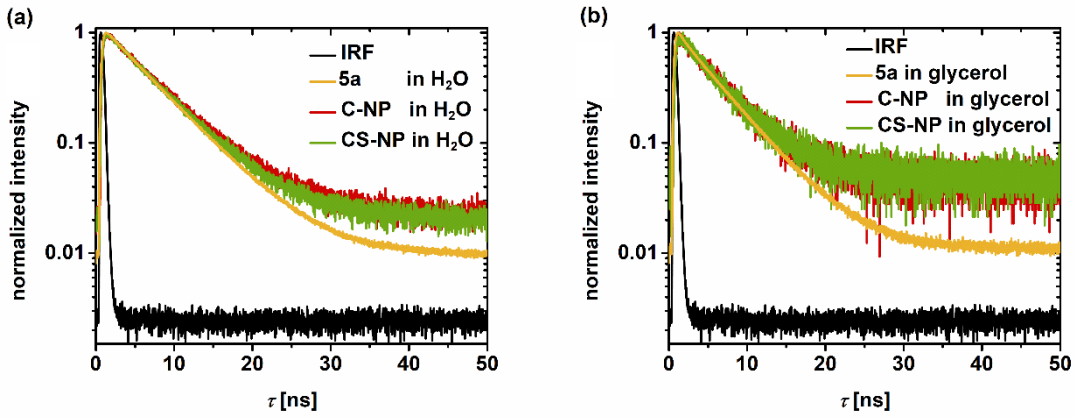

Figure S15: TCSPC-Histograms of core and core-shell nanoparticles in water (a) and after addition of glycerol (b) (λ_{ex}= 470 nm, λ_{em}= 500-550 nm), respectively.

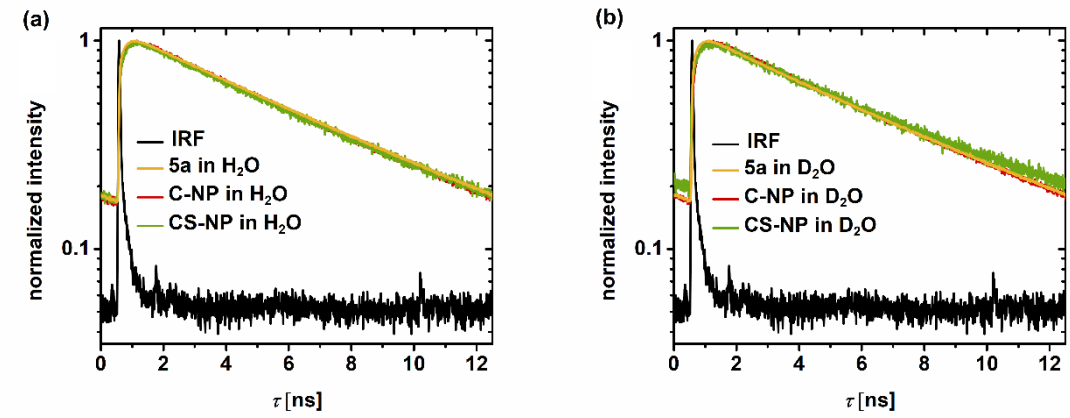

*Figure S16: TCSPC-Histograms of **5a**, core and core-shell nanoparticles in water (a) and deuterium oxide (b) after addition of HCl and DCl, respectively (λ_{ex}= 390 nm, λ_{em}= 500-550 nm).*

*Table S5: Reconvolution fitting of TCSPC data of **5a**, C-NP and CS-NP in water and deuterium oxide using biexponential function (λ_{ex}= 390 nm, λ_{em}= 500-550 nm), with the amplitude A.*

	τ_1 [ns]	A_1	τ_2 [ns]	A_2
5a in water	5.4	1	0.490	0.15
C-NP in water	4.4	1	0.139	-0.08
CS-NP in water	4.4	1	0.143	-0.06
5a in deuterium oxide	5.8	1	1.040	0.19
C-NP in deuterium oxide	4.5	1	0.139	-0.26
CS-NP in deuterium oxide	4.4	1	0.190	-0.19

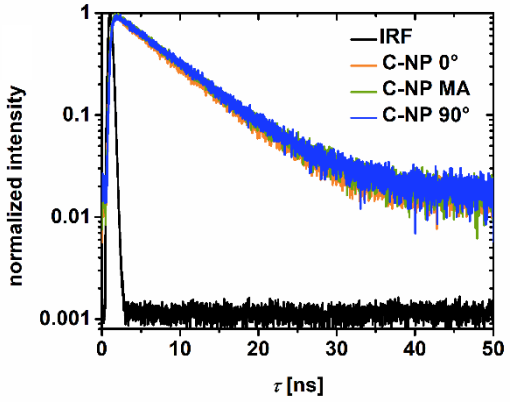

Figure S17: Time-dependent polarized decays of C-NP in water (λ_{ex} = 470nm, λ_{em} = 500-550 nm) (MA = magic angle ≈ 55°).

The fluorescence lifetime of **5a**, τ_{fl}, determined by TCSPC can be used to calculate the refractive index of the environment, $n_{calculated}$. The unknown refractive index n_x is calculated from the known refractive index of water and the corresponding fluorescence lifetime τ_{water} and τ_x according to equation (S4) [S6].

The refractive index determined by this method is in good agreement with the refractive index $n_{measured}$ as directly measured with an Abbe refractometer (Atago, 3T) (table S4). These data (τ_{fl} and $n_{measured}$) are plotted in figure 3a of the main manuscript.

$$n_x = n_{water} \cdot \sqrt{\frac{\tau_{water}}{\tau_x}} \quad \text{(S4)}$$

*Table S6: Comparison of $n_{calculated}$ and $n_{measured}$ of **5a** following the protocol in literature [S6]*

	τ_{fl} [ns]	$n_{calculated}$	$n_{measured}$
water	5.73	-	1.333
10% glycerol	5.62	1.346	1.350
15% glycerol	5.54	1.356	1.357
20% glycerol	5.51	1.361	1.364
30% glycerol	5.42	1.366	1.378
40% glycerol	5.31	1.386	1.390
50% glycerol	5.09	1.415	1.409
60% glycerol	5.11	1.413	1.422
70% glycerol	4.97	1.433	1.436
80% glycerol	4.84	1.451	1.452
90% glycerol	4.74	1.467	1.464

11. 2D and 3D fluorescence spectra after acidification

Fluorescence spectra of core nanoparticles (C-NP) and core-shell nanoparticles (CS-NP) (figure S18) were recorded in water after addition of hydrochloric acid (figure S18 a and c) and in deuterium oxide after addition of deuterium chloride (figure S18 b and d). The emission spectra of C-NP indicated within our time resolution, the immediate shift from the emission of the deprotonated form (RO^-) (not shown). 3D fluorescence spectra of core nanoparticles (C-NP) (figure S19a) and core-shell nanoparticles (CS-NP) (figure S19b) were recorded using Jasco spectrofluorometer FP-6500 (JASCO) in deuterium oxide after addition of deuterium chloride.

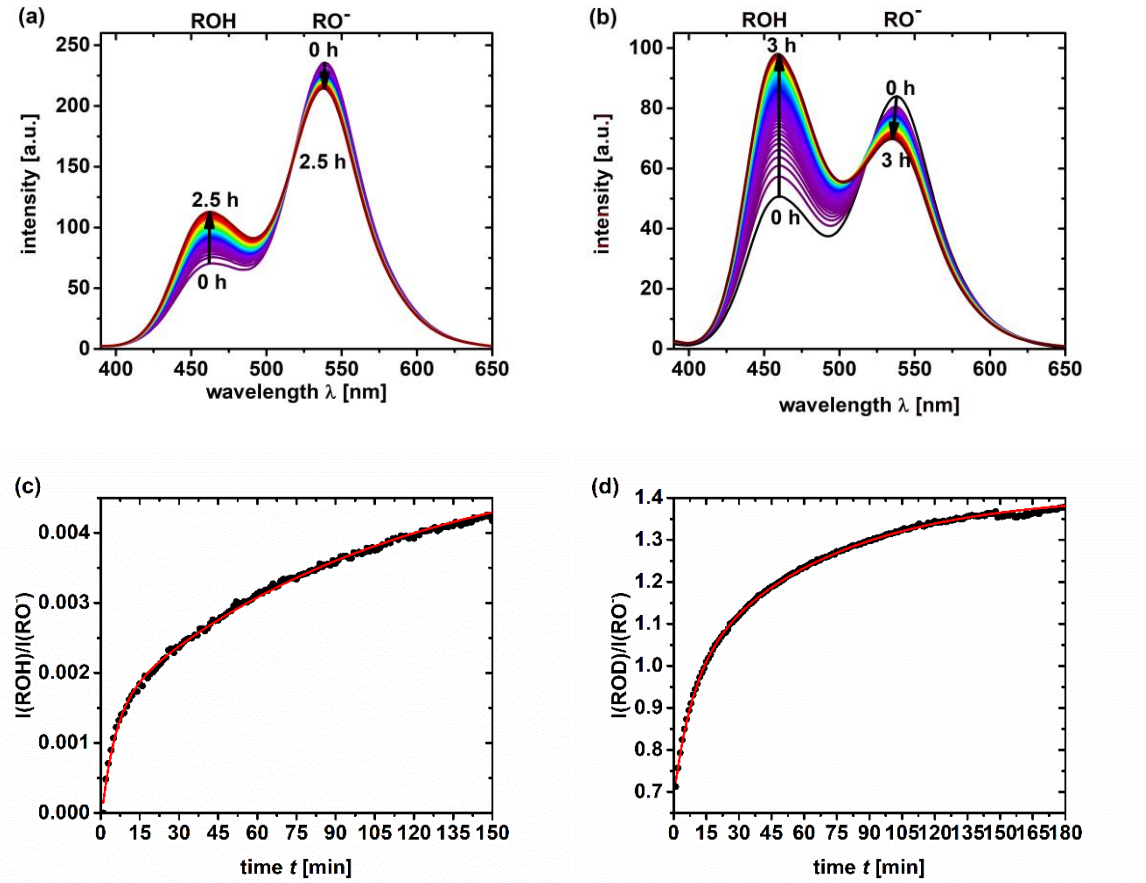

Figure S18: Emission spectra (λ_{ex} = 360 nm) of CS-NP in H_2O after addition of HCl (t= 2.5 h) (a) and in D_2O after addition of DCl (t= 3 h) (b), as well as kinetic of protonation in H_2O (c) and D_2O (d) with a biexponential decay curve function

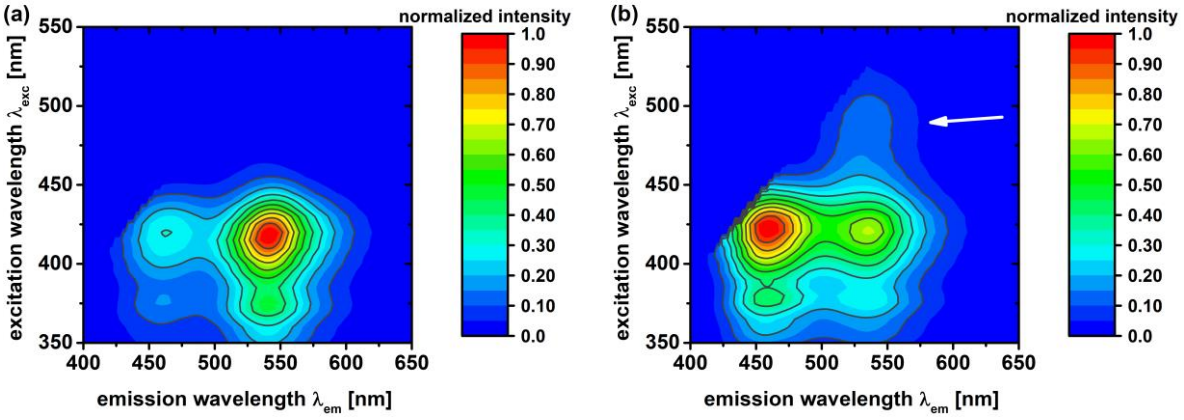

Figure S19: 3D fluorescence spectra of core nanoparticles (C-NP) (a) and core-shell nanoparticles (CS-NP) (white arrow: non-titratable fraction) (b) in deuterium oxide after addition of deuterium chloride.

12. Fluorescence correlation spectroscopy (FCS)

FCS-curves were registered using a custom built setup. A continuous-wave laser (Picarro, Solition, λ= 488 nm) with a beam diameter of 0.7 mm was used as excitation source. The laser was coupled into an inverted microscope (Axiovert 200, Zeiss) and deflected by a dichroic mirror (495 DRLP, Omega) into a water-immersion objective lens (PlanApo 63x, NA 1.2 WI, Zeiss). The beam was focused into a diffraction limited spot above the cover slide (0.17 ± 0.01 mm, Assistent). The laser power was varied between 25 µW and 3 mW, corresponding to an excitation intensity ranging from 7.5 kW cm^{-2} to 900 kW cm^{-2}. A drop of the modified nanoparticle solution, placed on top of the cover slip, served as sample. Emitted fluorescence was collected by the same objective, passed the dichroic mirror and was focused by the tube lens onto a 50 µm pinhole. After filtering through a band pass filter (HQ 570/60, AHF Analysentechnik), the light was divided into two beams by a 50:50 beam splitter. Photons were detected by two avalanche photodiodes (SPCM-14-AQR, Perkin-Elmer Optoelectronics) and the signals of these modules were cross-correlated by a hardware correlator (FLEX 02-01D/C, Correlator.com).

FCS was used with the intention to verify the successful incorporation of photoacid into the silica matrix via the diffusion time. Preliminary FCS-experiments at pH 8 (λ_{ex} = 488 nm) showed a pronounced intensity dependence, which can be used to analyse the photostability (figure S21). Unexpectedly, τ_{diff} close to the expected value ($\tau_{diff,exp}$(C-NP) ∼ 4 ms, $\tau_{diff,exp}$(C-NP) ∼ 5 ms) on the basis of equation (5) (in the main manuscript) and the hydrodynamic radius-date from figure S3 was noticed under no circumstances. We therefore repeated these experiments at pH 4.5 (figure S20) where a large fraction of all molecules resides in the neutral state (comparison to fluorescence excitation titration, figure S11 and S12). At a pH-value of 4.5 (and a laser intensity of 30 kW cm^{-2}) a diffusion time around 100 µs is typically observed for the used photoacid **5a**. The exhibited diffusion time of the core particles was, in contrast, ten times longer resulting in a value of around 1 ms. Furthermore, the diffusion time of the core shell nanoparticles lasted around 2 ms (figure S20). However, even at pH 4.5, the above expected diffusion times was not achieved. The obtained τ_{diff} around 1 ms correspond to a particle size of r_H= ∼4.5 nm.

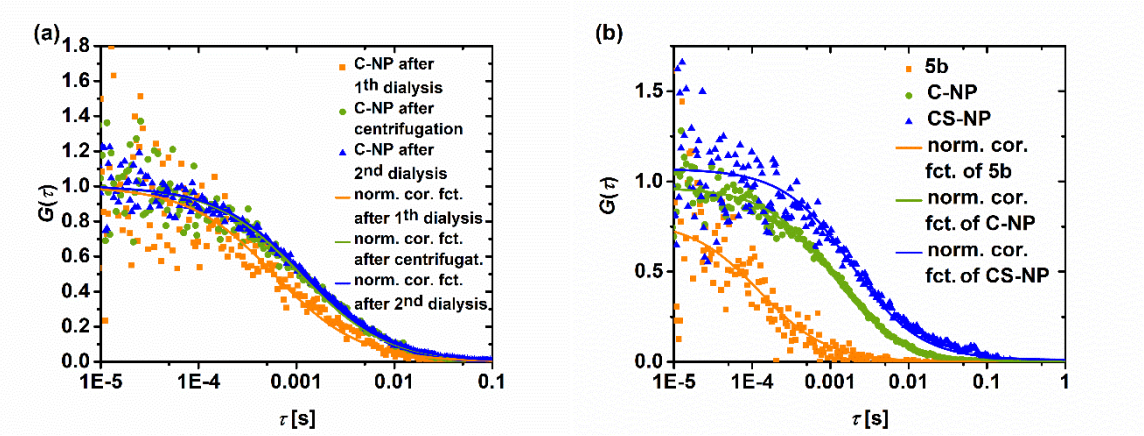

*Figure S20: Normalized FCS-curves of C-NP in water without and with further purification step (a) and unbound dye **5a**, core- and core-shell nanoparticle at pH 4.5 (b).*

The investigation of the photostability took place in buffer solution pH 4.5 (20 mM HPCE-buffer, sodium citrate) and the samples were excited with intensities spanning more than two orders of magnitude (7.5 to 903 kW cm^{-2}). In case of a pH-value of 8 (20 mM HPCE-buffer, sodium phosphate), the protonation can be ignored which simplifies the analysis. Analogous to the results of Hinkeldey et al. and Finkler et al.,[S7,S8] while ignoring the data points at highest intensities due to saturation phenomena, a decrease in the diffusion time with an increase in the excitation intensity was also observed. The determination of the photobleaching rate constant k_{bl} was carried out by Stern-Volmer analysis by plotting $\tau_{diff}(0)/\tau_{diff}(I)$ against the excitation intensity I [equation (S5)].[S9,S10]

$$\frac{\tau_{diff}(0)}{\tau_{diff}(I)} = 1 + k_{bl} \cdot \tau_{diff}(0) \cdot I \qquad \text{(S5)}$$

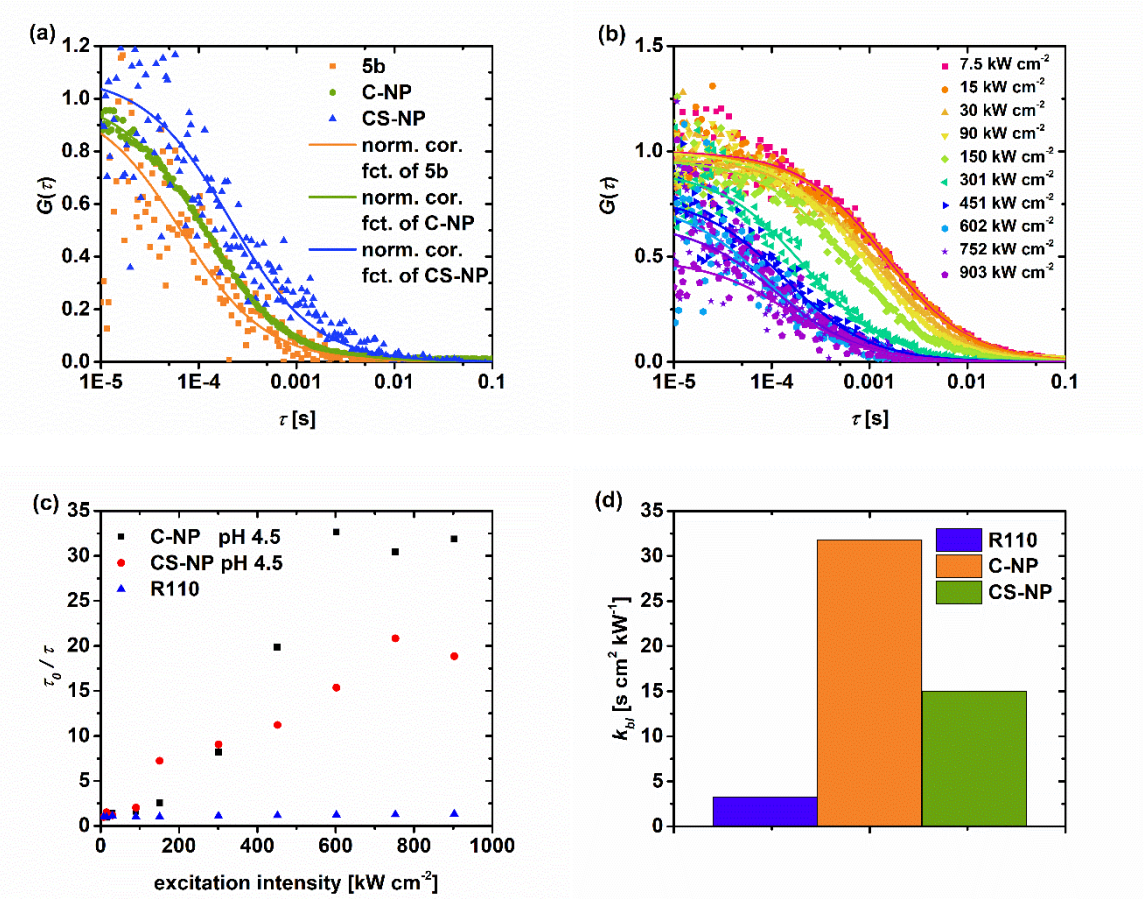

Figure S21: Investigation of the diffusion time and photostabilities of the core- (C-NP) and core-shell nanoparticles (CS-NP). Normalized FCS-curves of unbound dye, C-NP and CS-NP at pH 8 as well as at laser-intensity of 30 kW cm^{-2} (λ_{ex}= 488 nm) (a). Normalized FCS-curves of core nanoparticles at various excitation intensities (λ_{ex}= 488 nm) at pH 4.5 (b). Stern-Volmer type analyses at pH 4.5 for the determination of the photostability (c) and photobleaching rate constants at pH 4.5 (d).

Via FCS we found out that the synthesized C-NP have a higher photostability compared to the starting compound (figure S21d).

Generally, it seems that the photostability is higher at lower pH-value. This can be seen by the reduction of the diffusion time by the factor ten at pH 8 compared to pH 4.5 at the identical excitation intensity. The reason for this experimental observation is the permanent excitation of the deprotonated form, which predominates at pH 8. Therefore, the dye undergoes more photocycles in comparison to pH 4.5 in the same time. After cladding an unstained silica layer, the bleaching rate of the core-shell particles was halved in comparison to the core nanoparticles (figure S21d). Thus, it seems that the photoacid is more protected against light-driven, irreversible processes by the shell.

13. Solvatochromic behavior

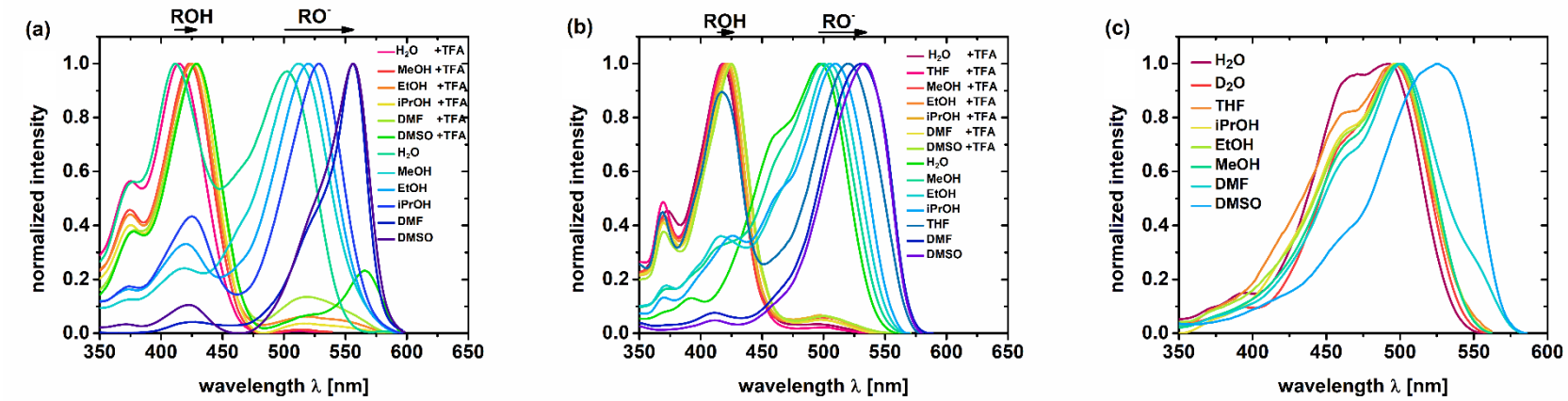

*Figure S22: Excitations spectra (λ_{em}= 590 nm) of **5a** (a), core (b) and core-shell nanoparticles (c) in various solvents.*

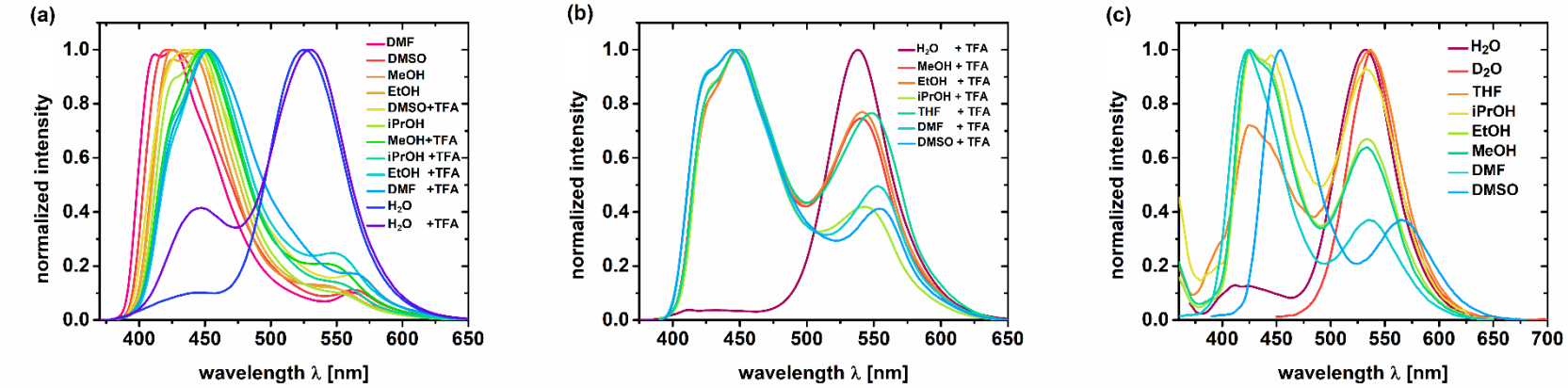

*Figure S23: Emission spectra (λ_{ex}= 350-380 nm) of **5a** (a) core (b) and core-shell nanoparticles (c) in various solvents.*

14. Steady-state quenching studies

Fluorescence quenching experiments were carried out to investigate the accessibility of the interior of the nanoparticles for external molecules (figure S24). Excitation spectra of core and core-shell nanoparticles were measured after aliquots of a stock solution of the quencher were added. The intensities *F* were analysed by Stern-Volmer-plots to determine the bimolecular quenching constant k_q [equation (S6)].[S5] In this expression $\tau_{fl,0}$ is the unquenched lifetime (see below) and *[Q]* the quencher concentration.

$$\frac{F_0}{F} = 1 + k_q \cdot \tau_{fl,0} \cdot [Q] \qquad \text{(S6)}$$

k_q describes the efficiency of quenching or the accessibility of the chromophores to the quencher. Values of k_q larger than $1 \cdot 10^{10}$ $M^{-1} s^{-1}$ indicate some type of binding interaction, which are not diffusion-controlled.[S5] We used three quenchers with different effective radii r_q , triethylamine ($r_q \leq 1$ nm), Cu(GlyGly) ($r_q \approx 3.6$ nm) as well as a cryptocyanine ($r_q \approx 7.8$ nm). Triethylamine is known to quench by PET resulting in the smallest effective radius,[S5] whereas the two others quenched via FRET with a larger effective quenching radius. The FRET radius of Cu(GlyGly) is similar to the system GFP-Cu^{2+} and cryptocyanine as organic dye with a strong electronic transition exhibits the largest FRET radius.[S11]

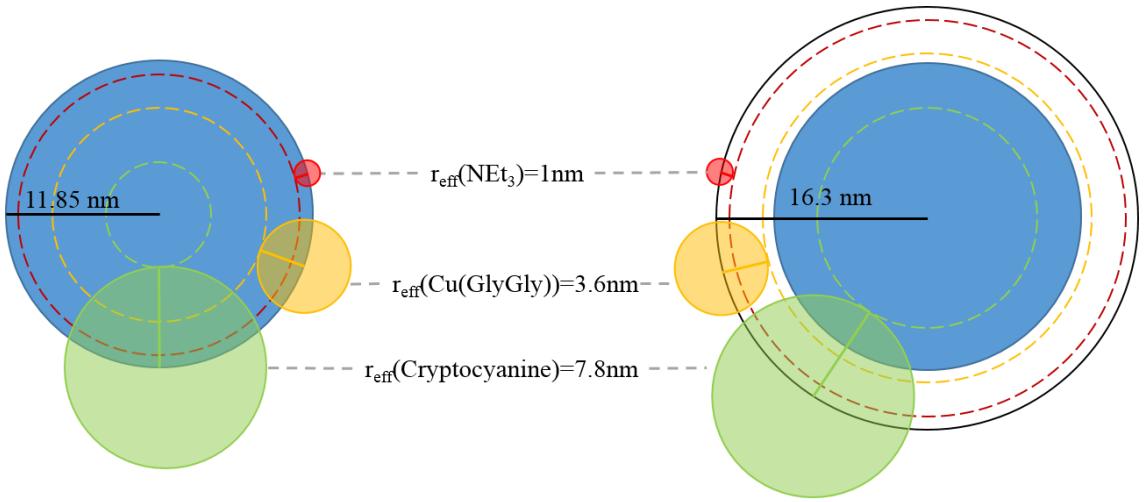

Figure S24: Effective radius of the quencher and the expected quenching behaviour on the core (left) resp. core-shell nanoparticles (right). For C-NP (left) we expected weak quenching with triethylamine (red), a pronounced by Cu(GlyGly) (yellow) and an almost complete quenching with cryptocyanine (green). In contrast, we expected for CS-NP (right) no fluorescence quenching by triethylamine (red) as well as Cu(GlyGly) (yellow). Only a moderate fluorescence quenching by cryptocyanine (green) was assumed.

All excitation spectra were measured by λ_{em} of 570 nm. The fluorescence quenching was carried out via PET and FRET. Triethylamin (10 mM) was used as the quencher for PET, Cu(GlyGly) (5 mM) and cryptocyanine (2.5 mM) for FRET.

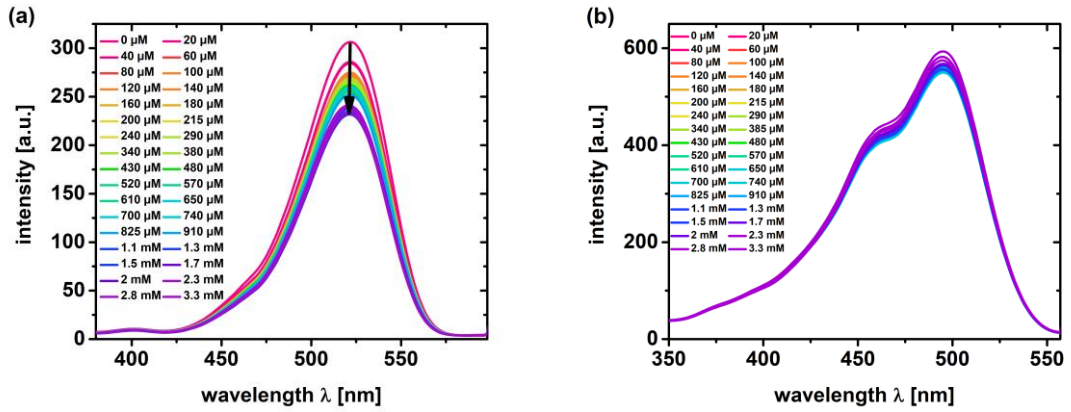

*Figure S25: Fluorescence quenching of **5a** (a) and C-NP (b) by PET via Triethylamine.*

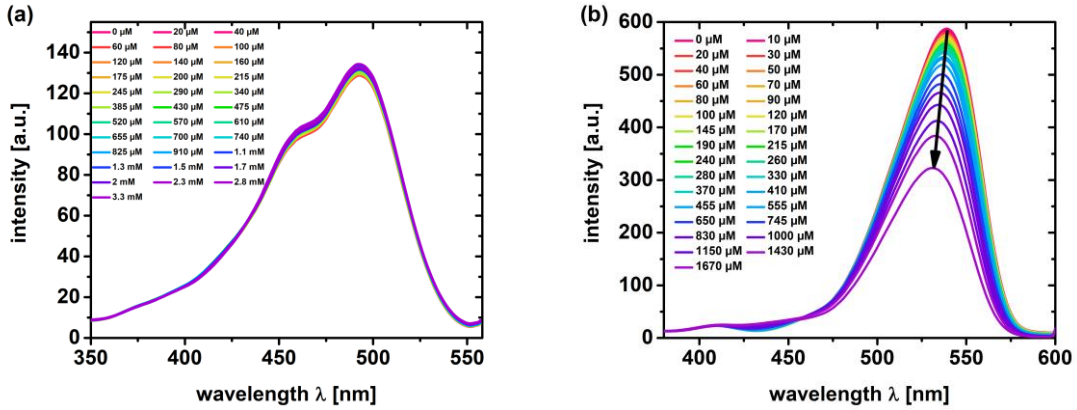

*Figure S26: Fluorescence quenching of CS-NP by PET via Triethylamine (a) and **5a** by FRET via Cu(GlyGly) (b).*

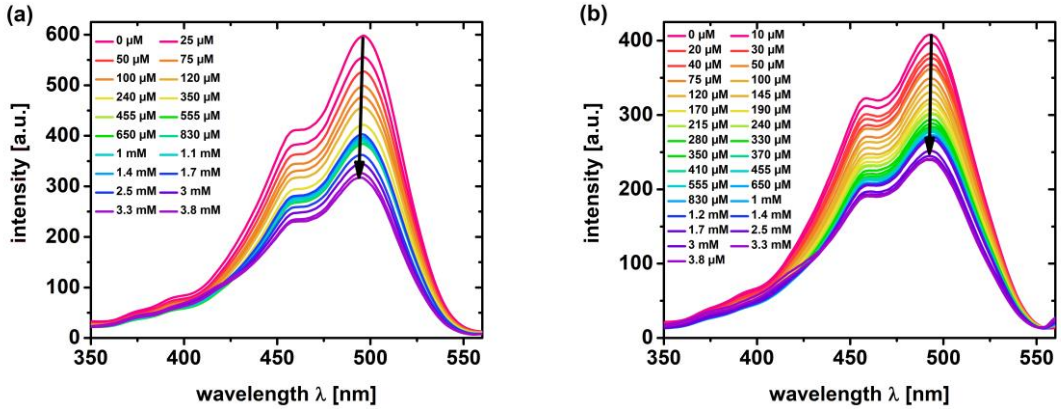

Figure S27: Fluorescence quenching of C-NP (a) and CS-NP (b) by FRET via Cu(GlyGly).

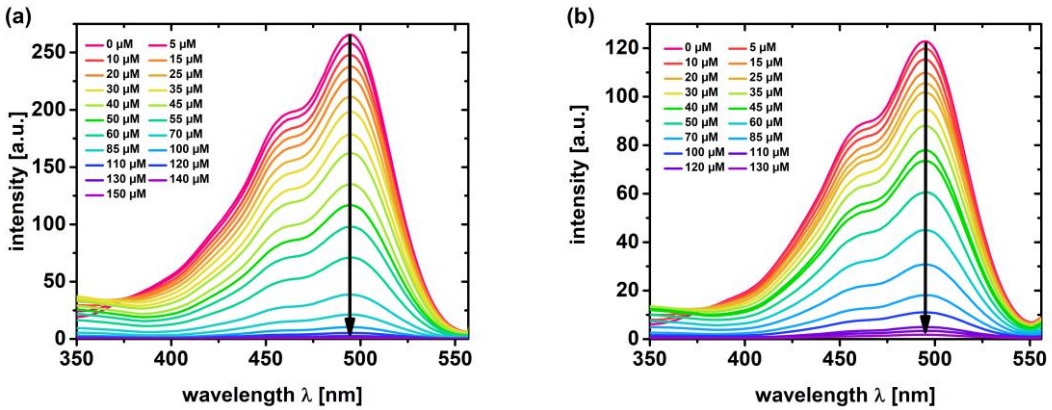

Figure S28: Fluorescence quenching of C-NP (a) and CS-NP (b) via Cryptocyanine.

*Table S7: Quenching constants k_q via PET and FRET of **5a**, core and core-shell particles.*

	r_{eff} [nm]	k_q(5a) [M^{-1} s^{-1}]	k_q(C-NP) [M^{-1} s^{-1}]	k_q(CS-NP) [M^{-1} s^{-1}]
Triethylamine	< 1	$1.68 \pm 0.17 \cdot 10^{11}$	-	-
Cu(GlyGly)	3.6	$4.35 \pm 0.09 \cdot 10^{11}$	$4.72 \pm 0.07 \cdot 10^{11}$	$4.48 \pm 0.28 \cdot 10^{11}$
Cryptocyanine	7.8	$5.87 \pm 0.37 \cdot 10^{12}$	$1.82 \pm 0.11 \cdot 10^{12}$	$1.70 \pm 0.08 \cdot 10^{12}$

The accessibility of the interior of both nanoparticle types was compared to the accessibility of unbound dye **5a** (table S7 and figure S29). By quenching experiments it was observed that **5a** was quenched with NEt_3 via PET and with Cu(GlyGly) via FRET (figure S25a and S26b). Unlike the unbound photoacid **5a**, quenching with NEt_3, is not detected for both nanoparticle varieties (figure S25b and S26a). Both C-NP and CS-NP, however, were prone to fluorescence quenching by both FRET acceptors Cu(GlyGly) and cryptocyanine, which reached saturation for the system with the smaller r_q-value (figure S27 and S29). In contrast, cryptocyanine was able to completely extinct the fluorescence of both C-NP and CS-NP (figure S28 and S29).

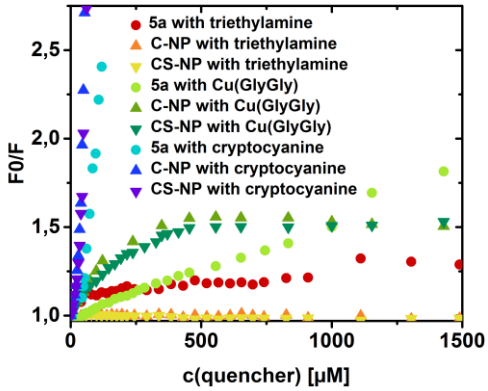

*Figure S29: Stern-Volmer type analysis of quenching of **5a**, C-NP and CS-NP via PET and FRET.*

15. Steady-state fluorescence anisotropy measurements

According to the work of Perrin, the anisotropy *r* is related inversely proportional to the temperature (equation 1 and equation 2 in the main manuscript) [S5]. Based on this dependence Wahl and Weber investigated the mobility of a fluorophore by plotting the quotient of temperature *T* and viscosity *η* versus the reciprocal of the anisotropy *r* (Perrin-Weber plot).[S12,S13] In case of a rigidly incorporation of the chromophore in the system, the resulting Perrin-Weber plot is expected to be a straight-line. If the fluorophore has a local mobility, however, than the slope of the Perrin-Weber plot would increase at lower *T*/*η* values and a kink would be expected.

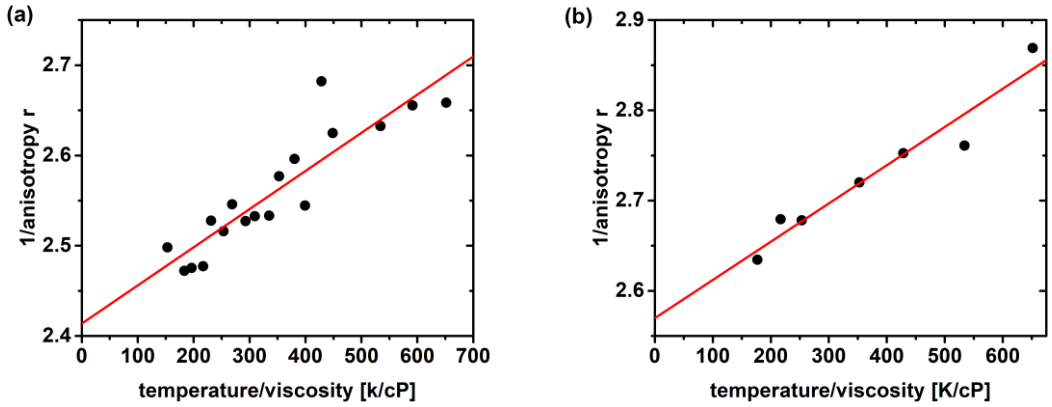

Figure S30: Temperature-dependent anisotropy measurements of the core nanoparticles (a) and core-shell nanoparticles (b).

16. Cell experiments

16.1. Transmission Electron Microscopy (TEM)

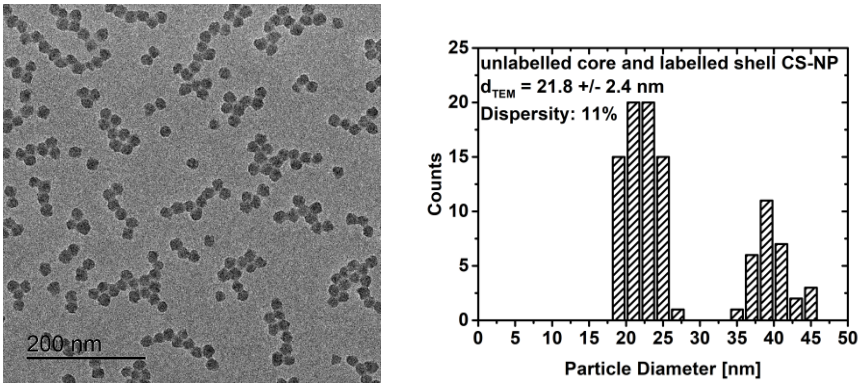

Figure S31: TEM image and histogram of core-shell nanoparticles with unlabelled core and labelled shell in H_2O (d_{TEM}= 27.3 ± 8.4 nm).

16.2. Dynamic Light Scattering (DLS)

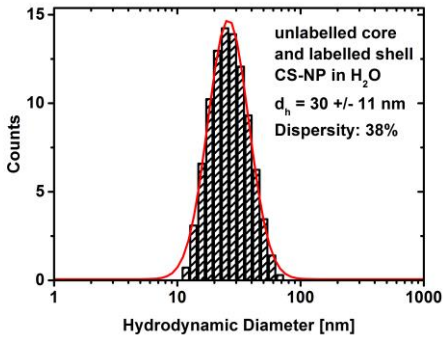

Figure S32: DLS analysis of core-shell nanoparticles with unlabelled core and labelled shell in H_2O (d_h= 30 ± 11 nm).The mean hydrodynamic diameter (d_h) is expressed as the lognormal distribution for the intensity density and the dispersity (p) is calculated with the formula $= {}^{\sigma}/_{\mu}$; σ = standard deviation, μ = mean value.

Table S8: Measured diameter of core-shell nanoparticles with unlabelled core and labelled shell by TEM and DLS

	$d_{measured}$ (CS-NP) [nm]	**dispersity (CS-NP) [%]**
d_{TEM} (CS-NP)	27.3 ± 8.4	30
d_h (CS-NP) (intensity distribution)	30 ± 11	38
z-average	27	22

16.3. Confocal fluorescence images of A549

The human alveolar epithelial cell line A549 (ACC 107) was obtained from German Collection of Microorganisms and Cell Culture (DSMZ, Braunschweig, Germany). Cells were maintained in Dulbecco's modified Eagle's medium (DMEM), supplemented with 10 % (v/v) fetal bovine serum (PAN-Biotech GmbH, Aidenbach, Germany). The cells were kept at 37 °C in an incubator under humidified atmosphere with 9% CO_2 and dislodged using Cellstripper (Corning, Wiesbaden, Germany).

For cell experiments, A549 cells were seeded at a density of 10^5 cells mL^{-1} with a final volume of 500 µL per well in a 4-chamber cell culture dish with glass bottom (CELLview™, Greiner Bio-One, Frickenhausen, Germany) and allowed to attach for 24 h. Before addition of particle suspension, nanoparticle dispersions of CS-NP with unlabelled core and labelled shell were freshly prepared in complete cell culture medium. After removal of the medium, cells were incubated with the CS-NP dispersion at a concentration of 100 µg SiO_2 per mL for 6 or 24 hours. Untreated cells, exposed to medium without nanoparticles, served as a control.

After nanoparticle exposure, localization of CS-NP was investigated by live cell imaging. Therefore, A549 cells were stained either by fluorescent wheat germ agglutinin conjugate with tetramethylrhodamine (WGA-TRITC, Thermo Fisher Scientific) for 10 min at 37 °C to label plasma membrane. On the other hand A549 cells were stained by Lysotracker (LysoTracker™ Red DND-99, Thermo Fisher Scientific) for 3 h at 37 °C, which has high selectivity for acidic organelles as lysosomes. Cell labelling and nanoparticle localization was analyzed at 37 °C and 9% CO_2. A confocal laser scanning microscope (Zeiss LSM 880, Carl Zeiss, Jena, Germany) using a Plan-Apochromat 63x/1.4 oil immersion objective was used to generate images. WGA-TRITC and Lysotracker were imaged using 543 nm excitation laser line. Their fluorescence (indicated in red) was detected at 565-590 nm with PMT-detector. Nanoparticle fluorescence of ROH (indicated in blue) was detected at λ_{ex}= 405 nm and λ_{em}= 510-550 nm, while of RO^- (indicated in green) at λ_{ex}= 488 nm and λ_{em}= 510-550 nm. Images were finally processed using the image processing software ImageJ.

16.4. Confocal fluorescence images of A549 – Control experiments

In control experiments (figure S33 and S34), weak autofluorescence was especially found in the green channel after 24 h, presumably localized in acidic compartments like lysosome.

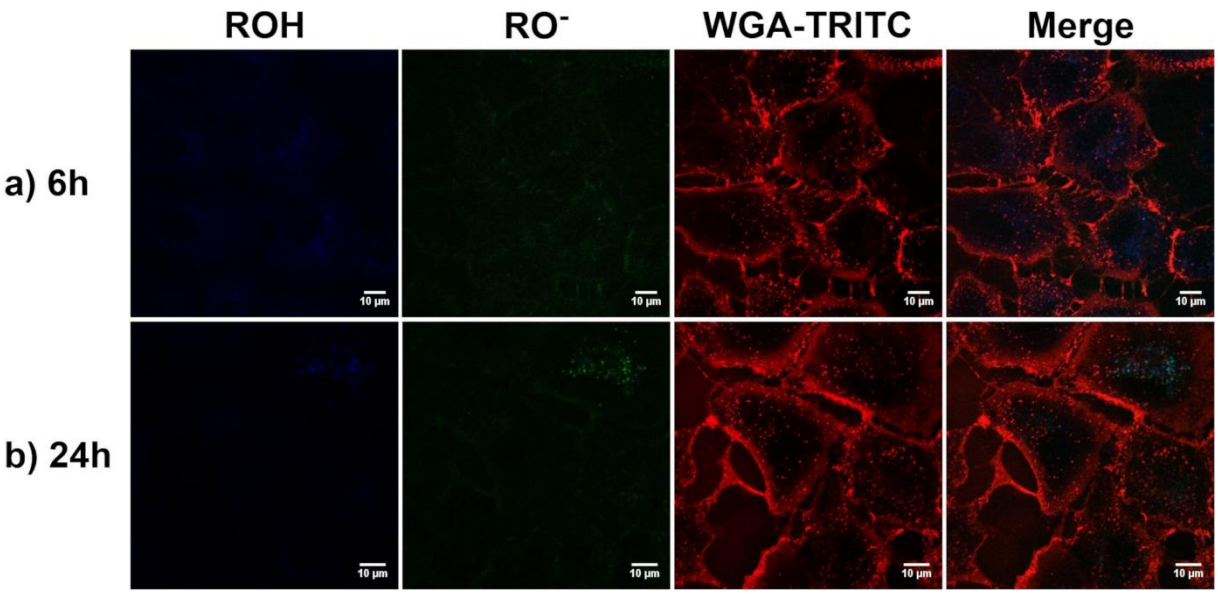

Figure S33: Confocal fluorescence images of A549 cells after 6 h (a) and 24 h (b) without nanoparticles treatment. The plasma membrane was stained with tetramethylrhodamine WGA (WGA-TRITC). The images in the first column show the protonated form (ROH, blue) (λ_{ex}= 405 nm, λ_{em}= 510-550 nm) and in the second column the deprotonated form (RO^-, green) (λ_{ex}= 488 nm, λ_{em}= 510-550 nm). The pictures in the third column display the staining with WGA-TRITC (red) (λ_{ex}= 543 nm, λ_{em}= 570-650 nm). In the fourth column are the merged images of ROH, RO^- and WGA-TRITC (blue, green and red).

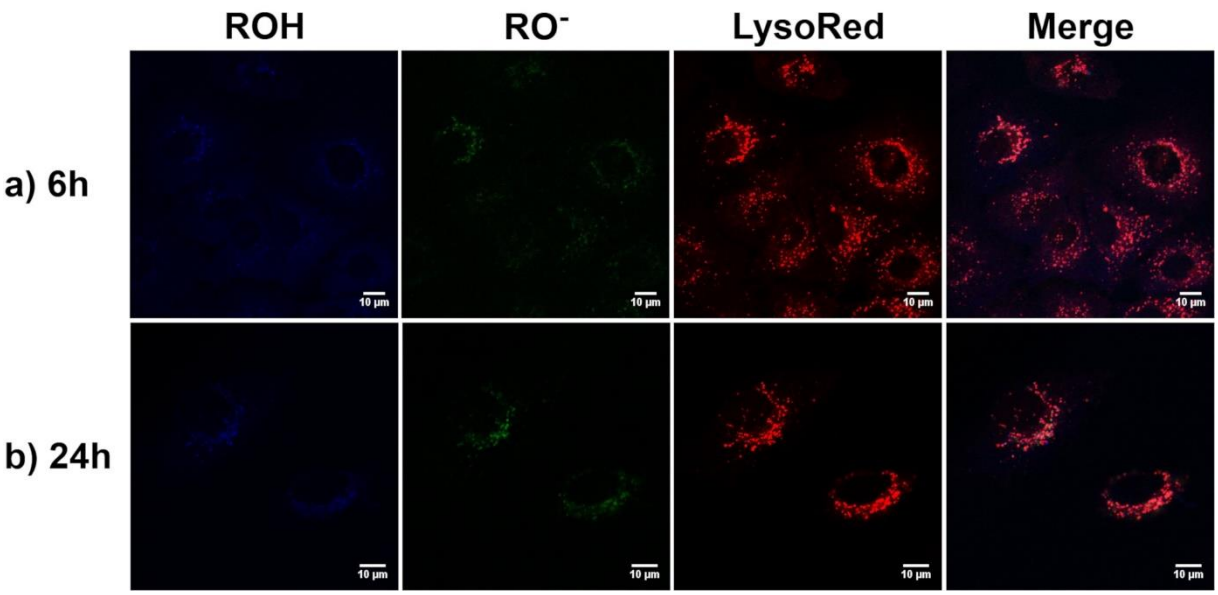

Figure S34: Confocal fluorescence images of A549 cells after 6 h (a) and 24 h (b) without nanoparticles treatment. The lysosome was stained with LysoTracker Red DND-99 (LysoRed). The images in the first column show the protonated form (ROH, blue) (λ_{ex}= 405 nm, λ_{em}= 510-550 nm) and in the second column the deprotonated form (RO^-, green) (λ_{ex}= 488 nm, λ_{em}= 510-550 nm). The pictures in the third column display the staining with LysoRed (red) (λ_{ex}= 543 nm, λ_{em} =570-650 nm). In the fourth column are the merged images of ROH, RO^- and LysoRed (blue, green and red).

17. NMR and mass spectra

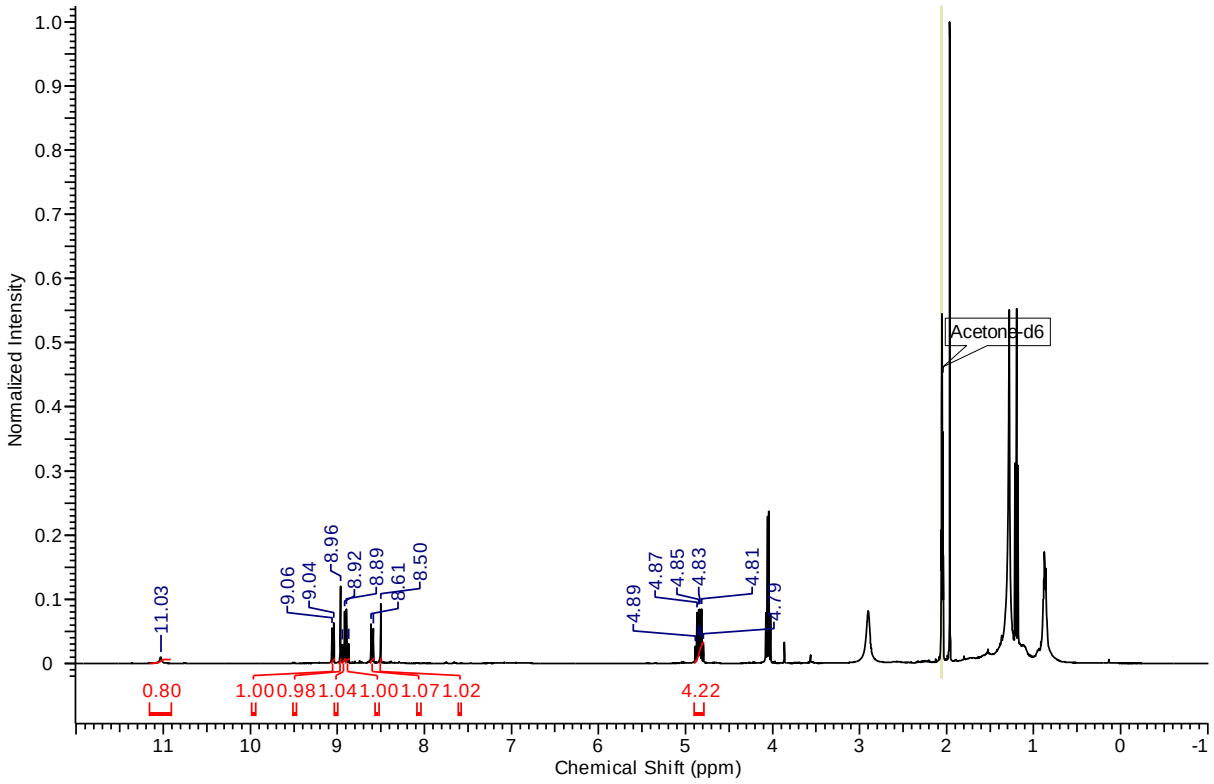

*Figure S35: ^{1}H-NMR (400.13 MHz, acetone-d_6, 25°C) spectrum of compound **2**.*

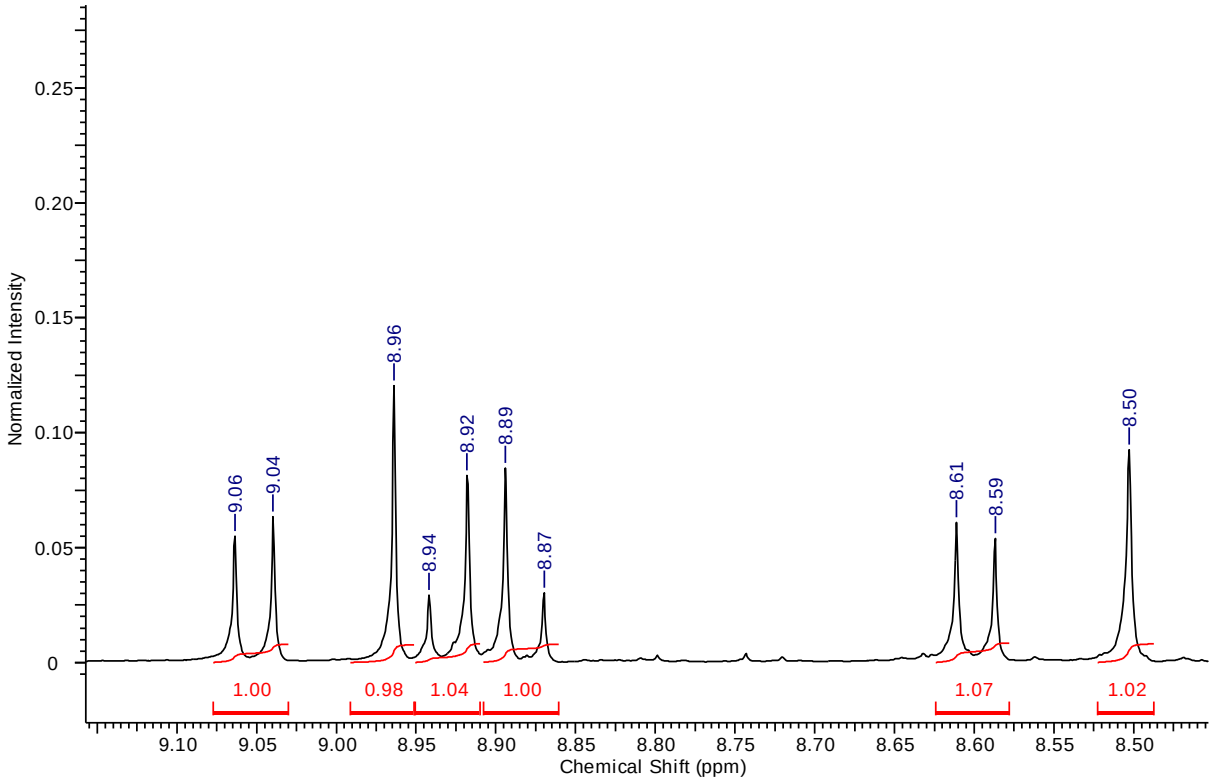

*Figure S36: ^{1}H-NMR (400.13 MHz, acetone-d_6, 25°C) spectrum of compound **2** (zone 1).*

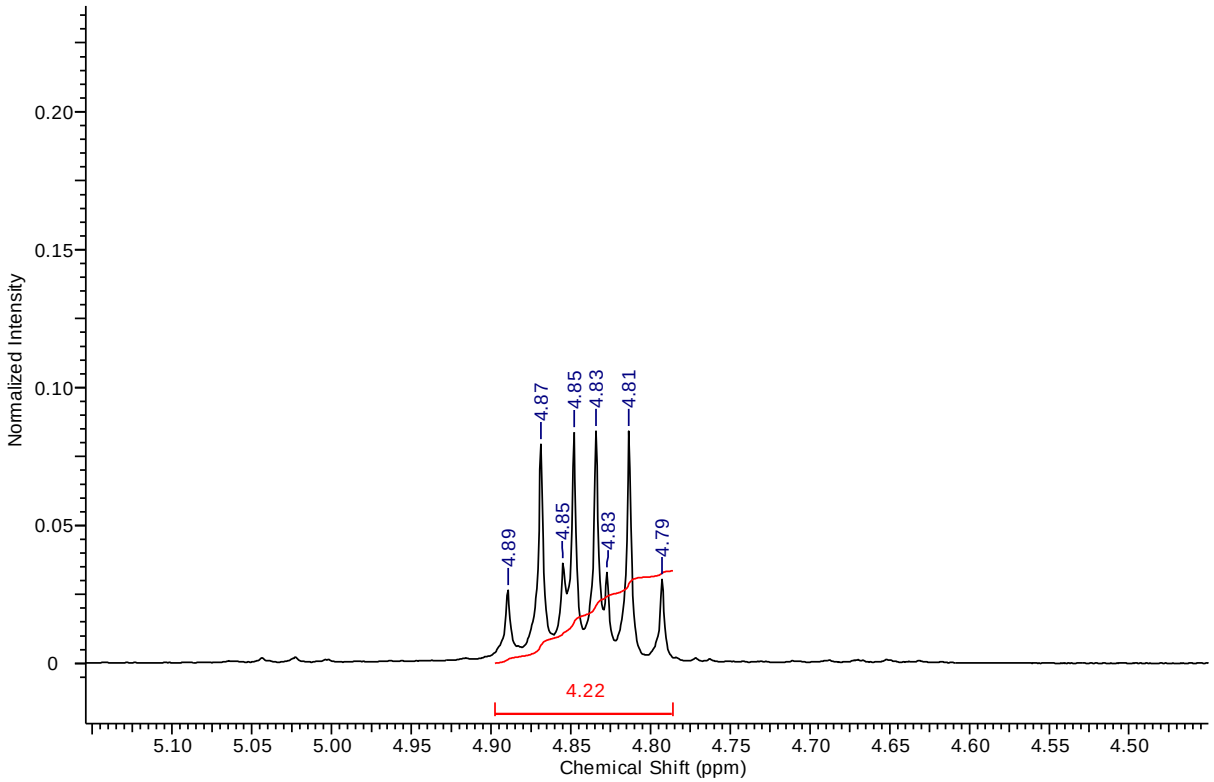

*Figure S37: ^{1}H-NMR (400.13 MHz, acetone-d_6, 25°C) spectrum of compound **2** (zone 2).*

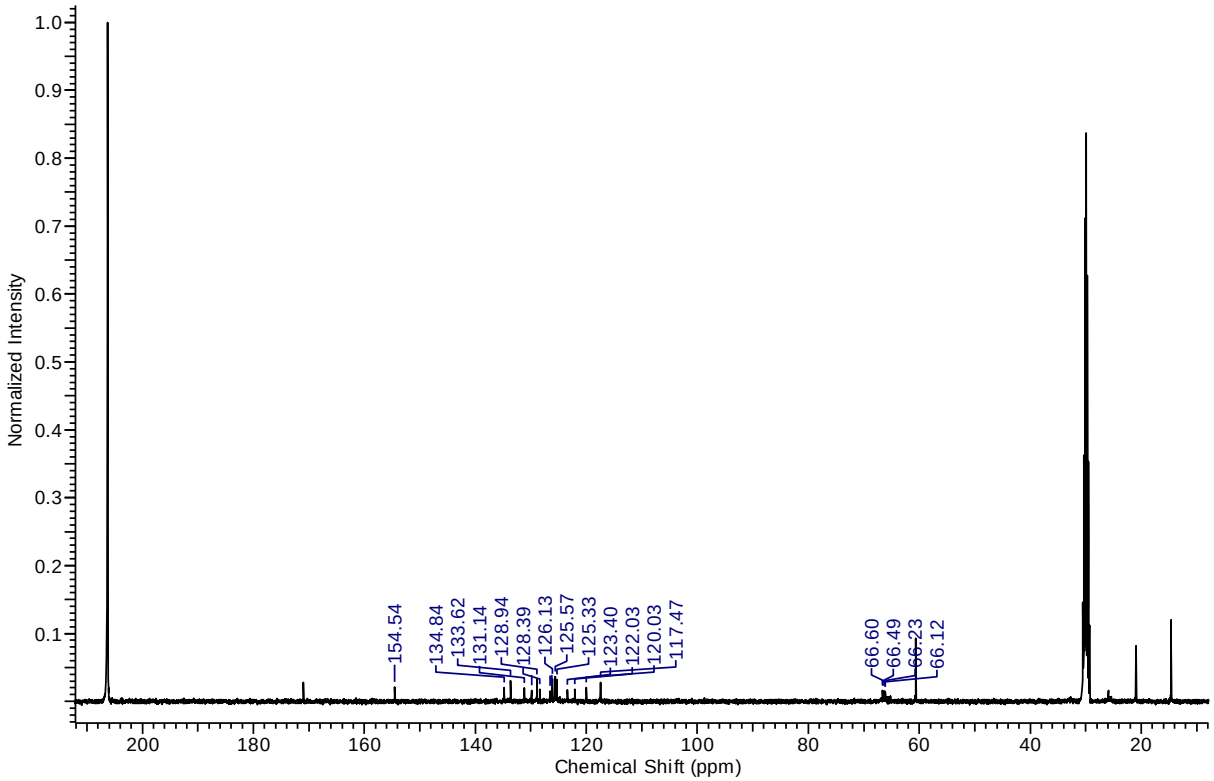

*Figure S38: ^{13}C-NMR (100.61 MHz, acetone-d_6, 25°C) spectrum of compound **2**.*

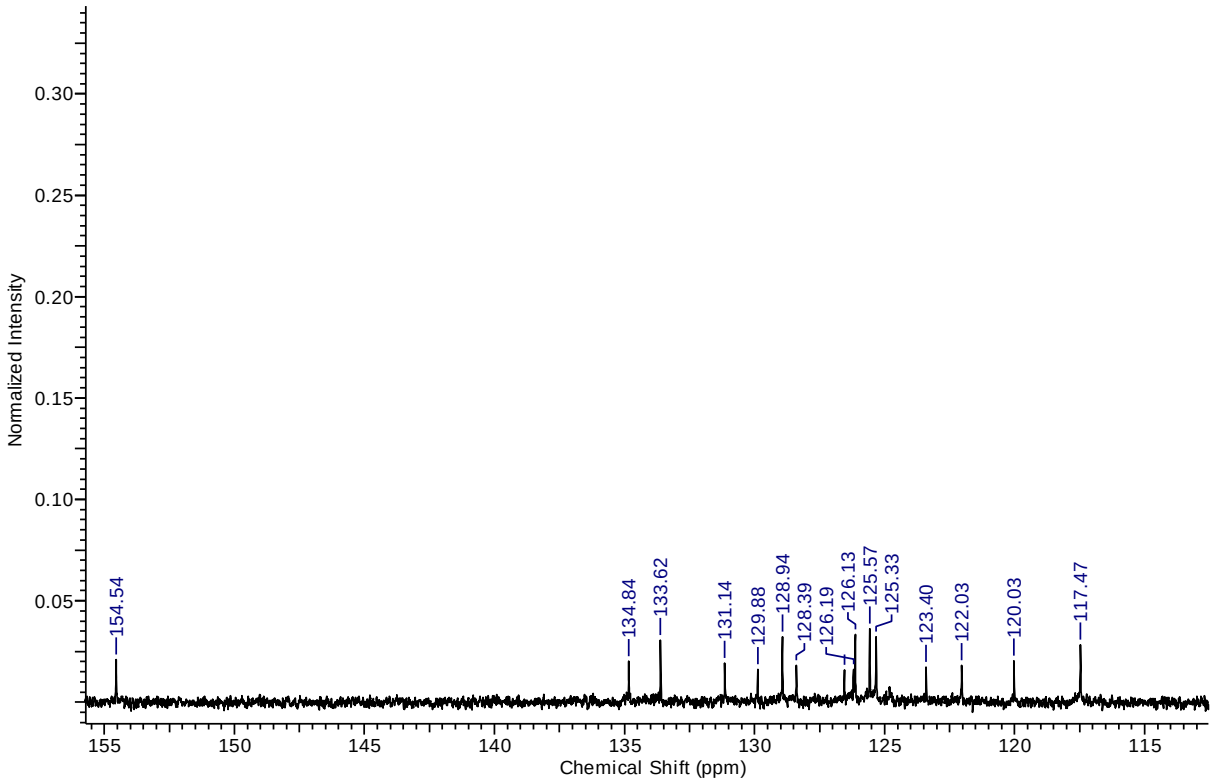

*Figure S39: ^{13}C-NMR (100.61 MHz, acetone-d_6, 25°C) spectrum of compound **2** (zone 1).*

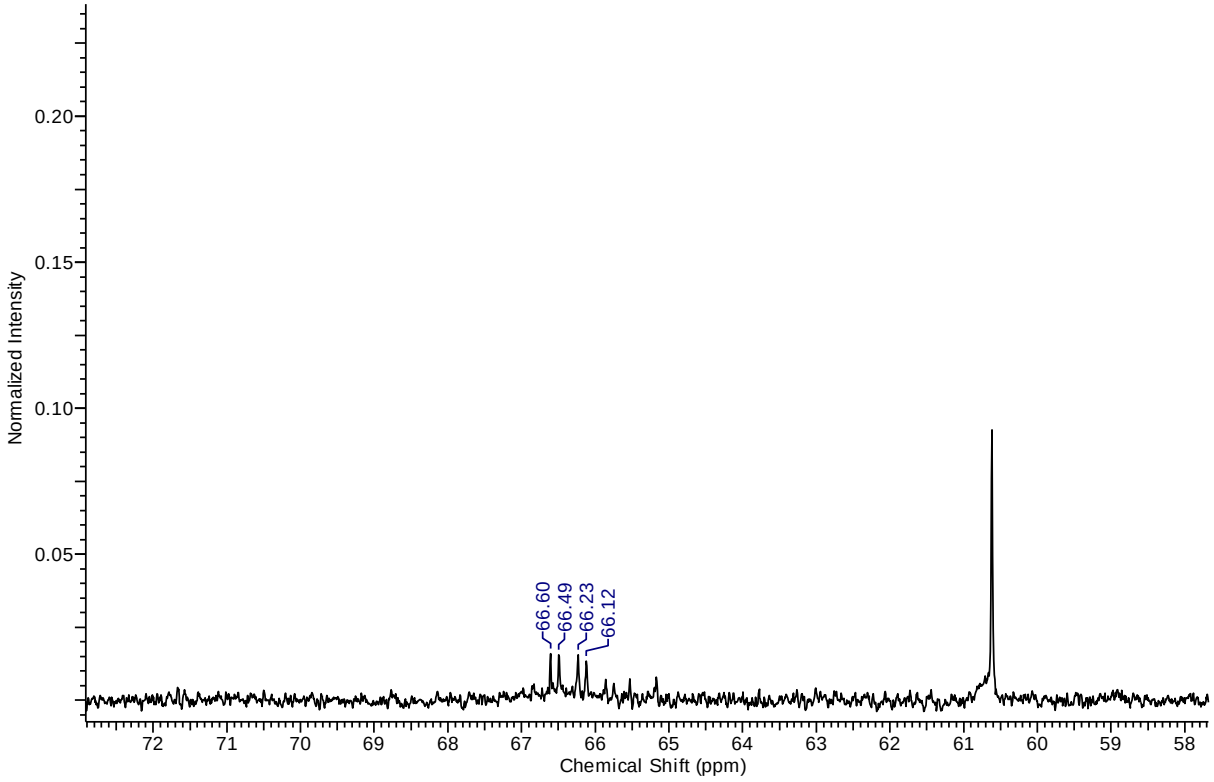

*Figure S40: ^{13}C-NMR (100.61 MHz, acetone-d_6, 25°C) spectrum of compound **2** (zone 2).*

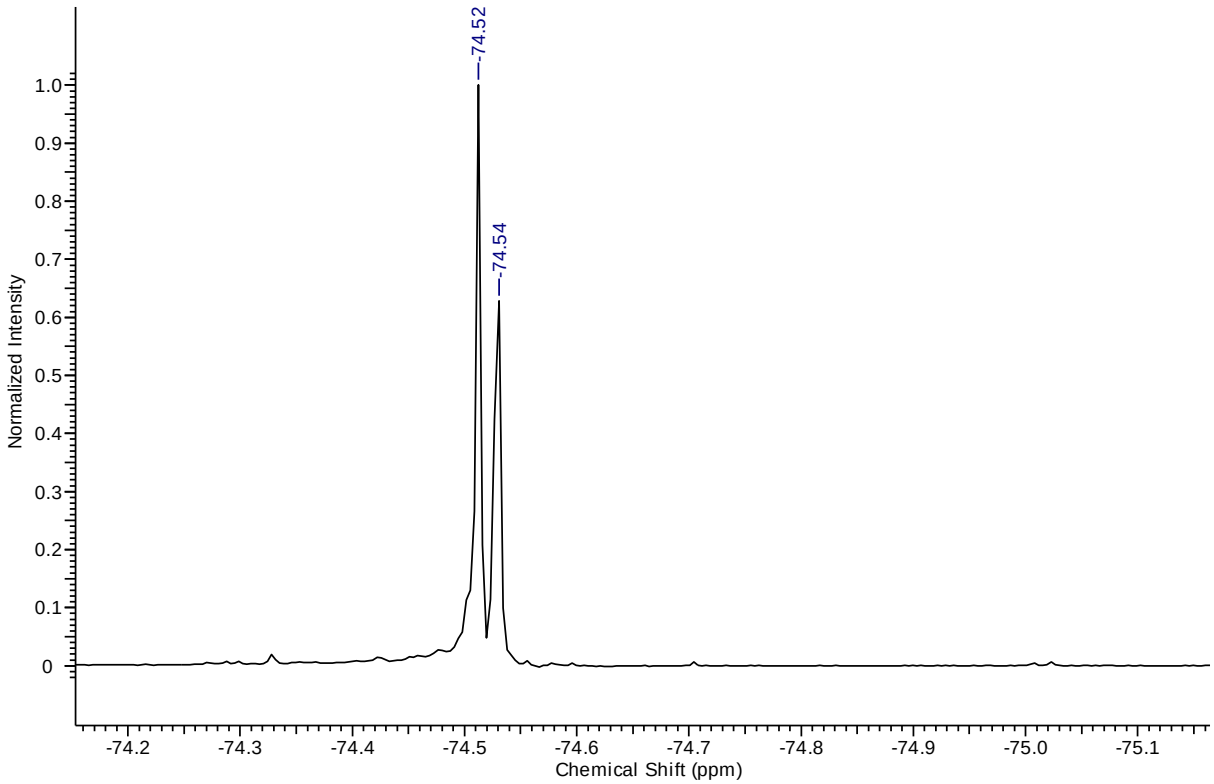

*Figure S41: ^{19}F-NMR (376.5 MHz, acetone-d_6, 25°C) spectrum of compound **2**.*

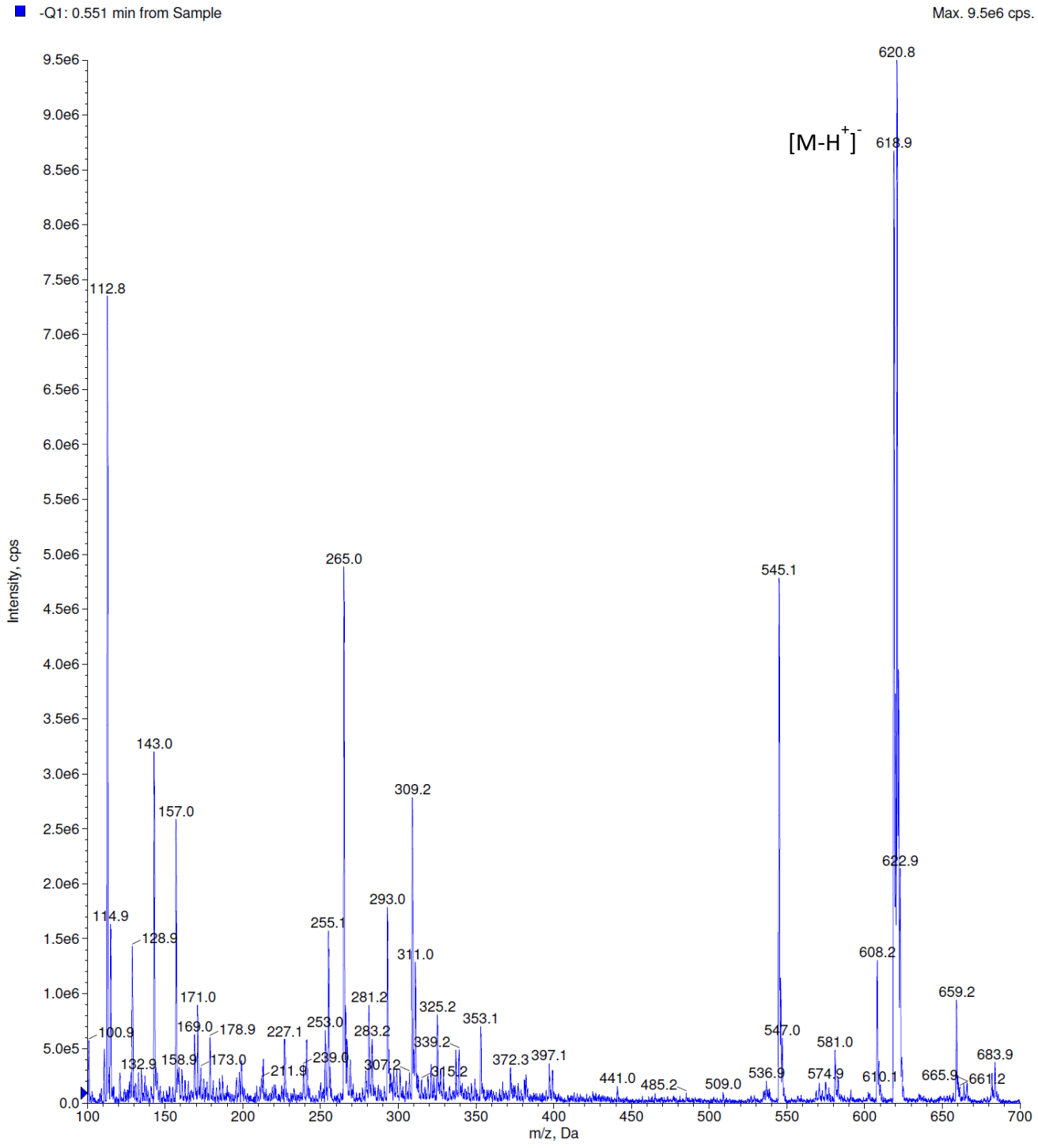

*Figure S42: Mass spectrum (ESI, negative ion mode) of **2**.*

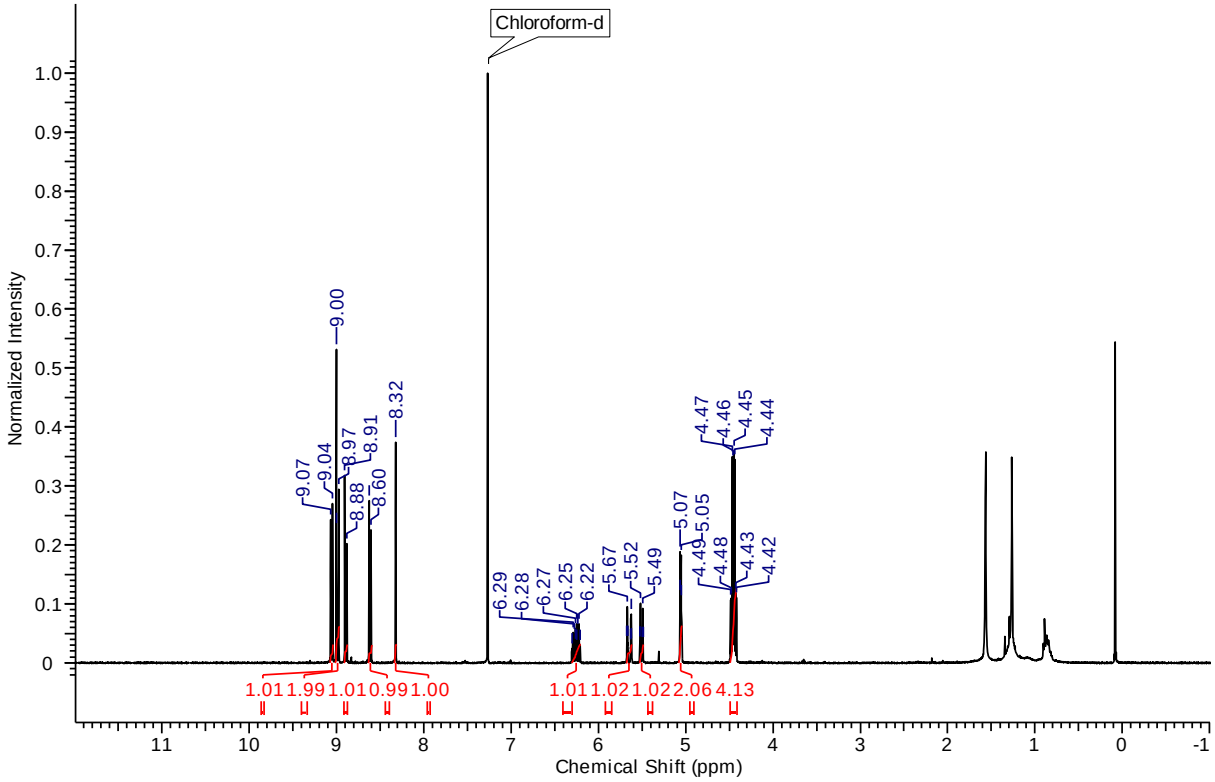

*Figure S43 [1]H-NMR (400.13 MHz, chloroform-d, 25°C) spectrum of compound **3**.*

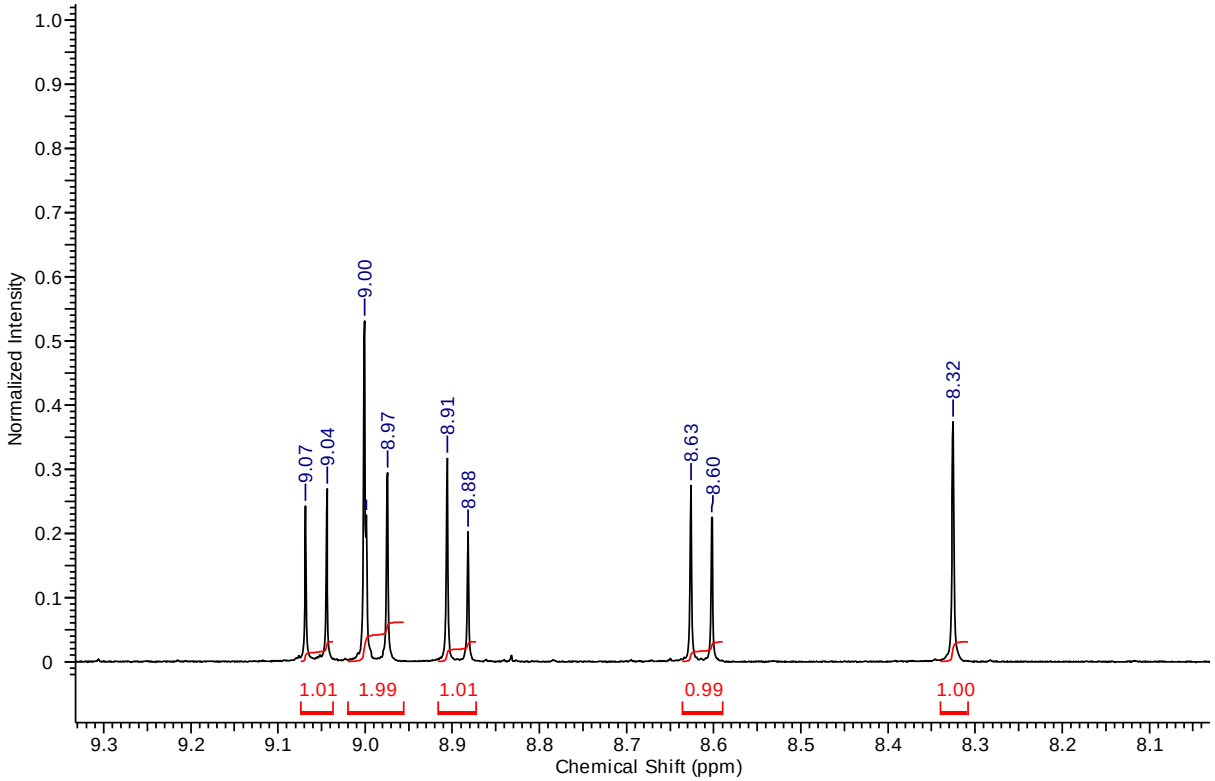

*Figure S44: [1]H-NMR (400.13 MHz, chloroform-d, 25°C) spectrum of compound **3** (zone 1).*

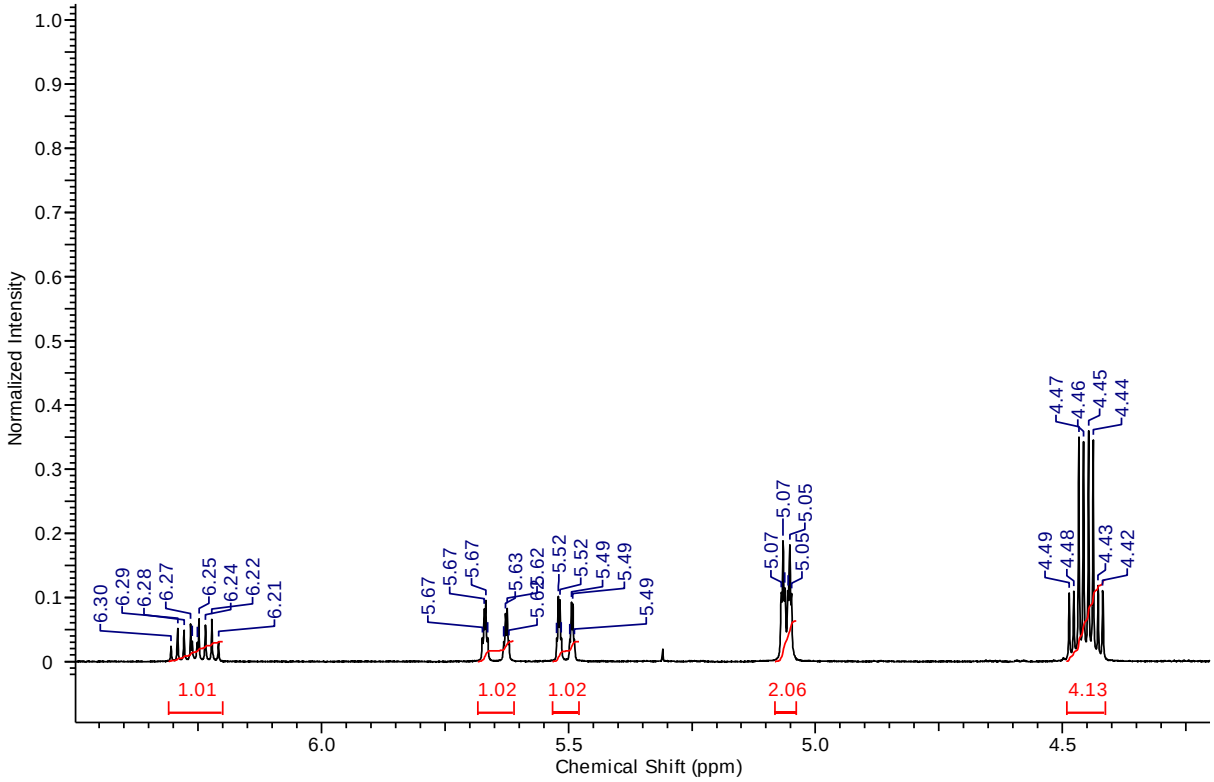

*Figure S45: [1]H-NMR (400.13 MHz, chloroform-d, 25°C) spectrum of compound **3** (zone 1).*

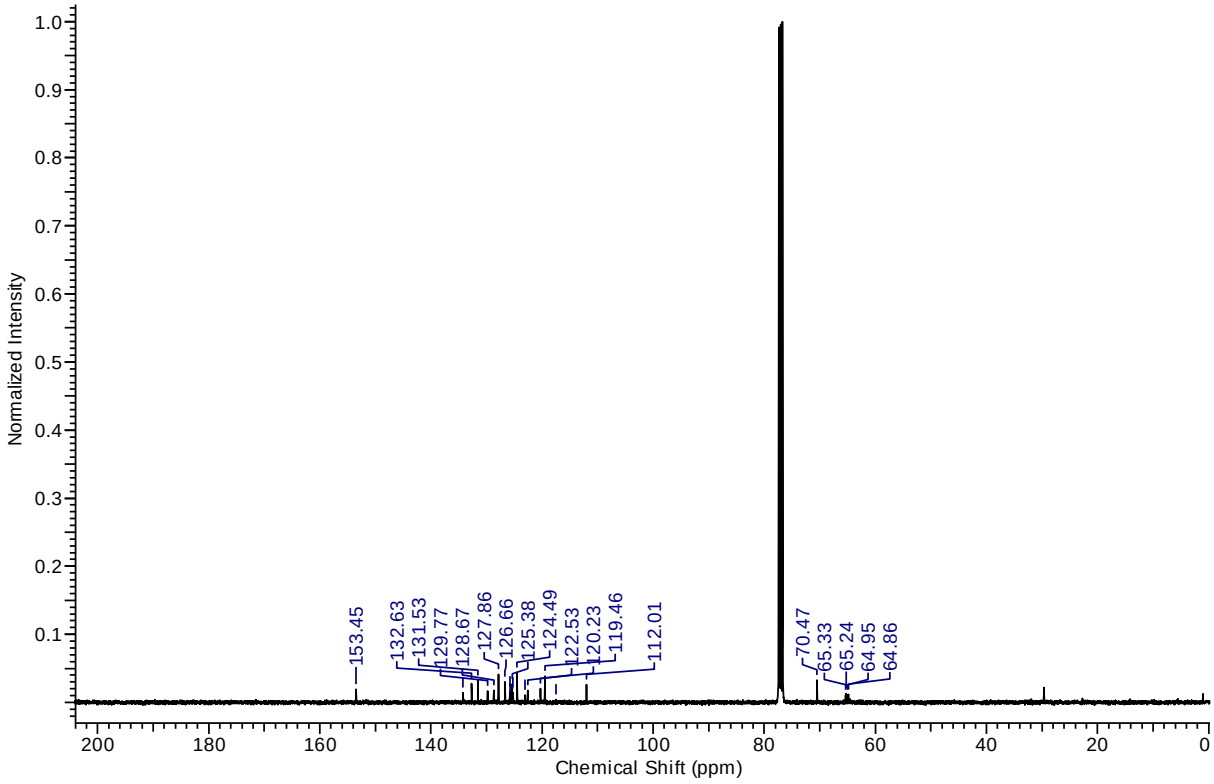

*Figure S46: [13]C-NMR (100.61 MHz, chloroform-d, 25°C) spectrum of compound **3**.*

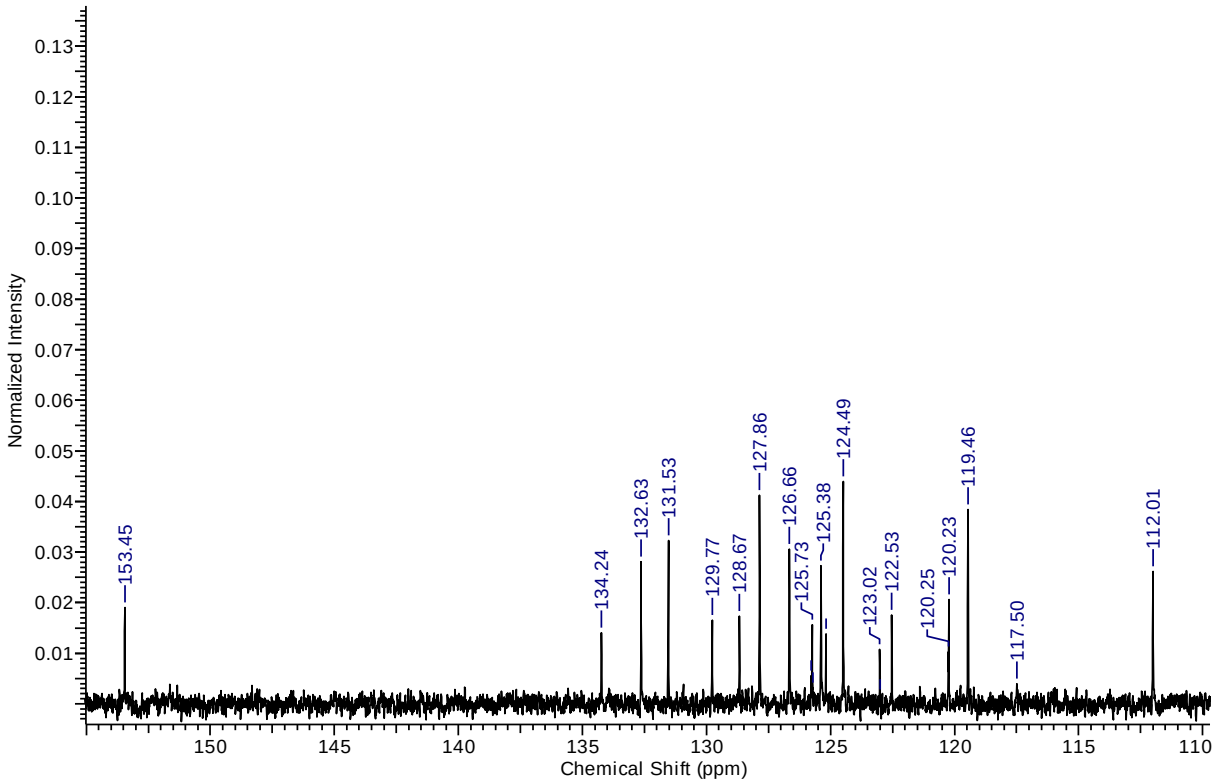

*Figure S47: ^{13}C-NMR (100.61 MHz, choroform-d, 25°C) spectrum of compound **3** (zone 1).*

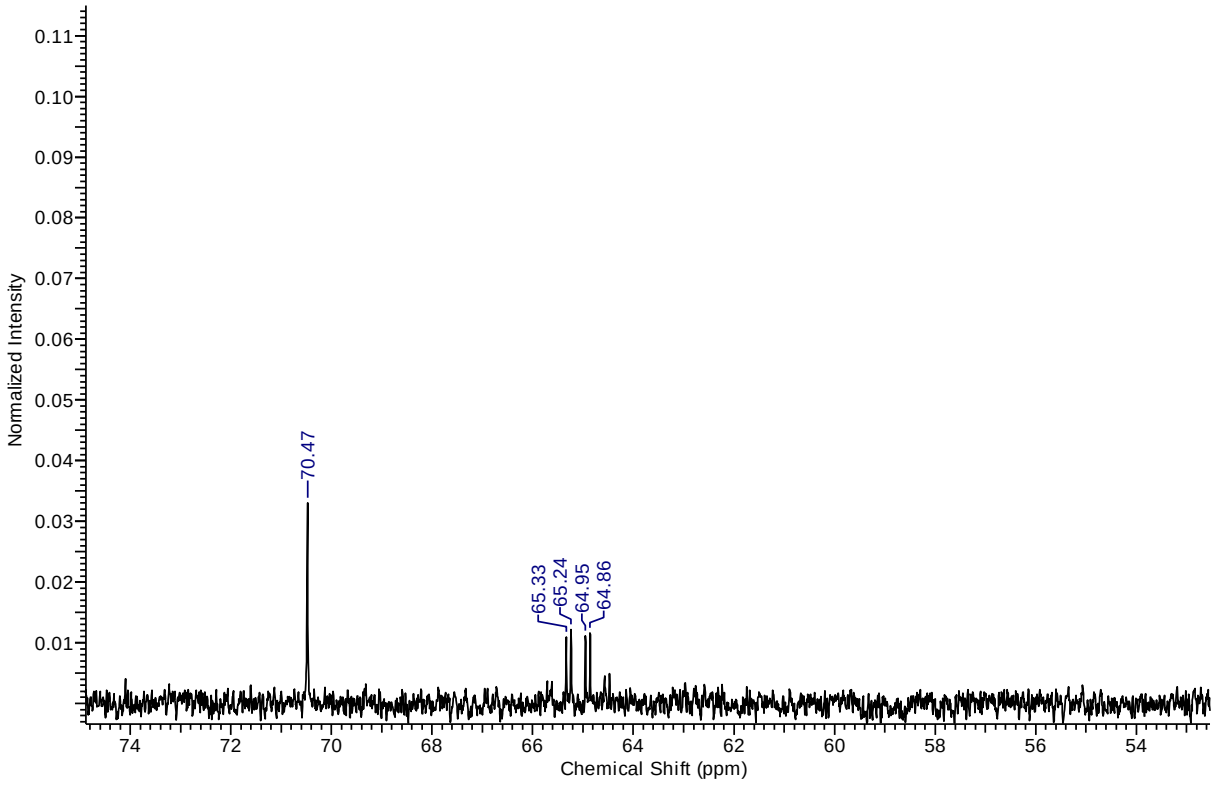

*Figure S48: ^{13}C-NMR (100.61 MHz, chloroform-d, 25°C) spectrum of compound **3** (zone 2).*

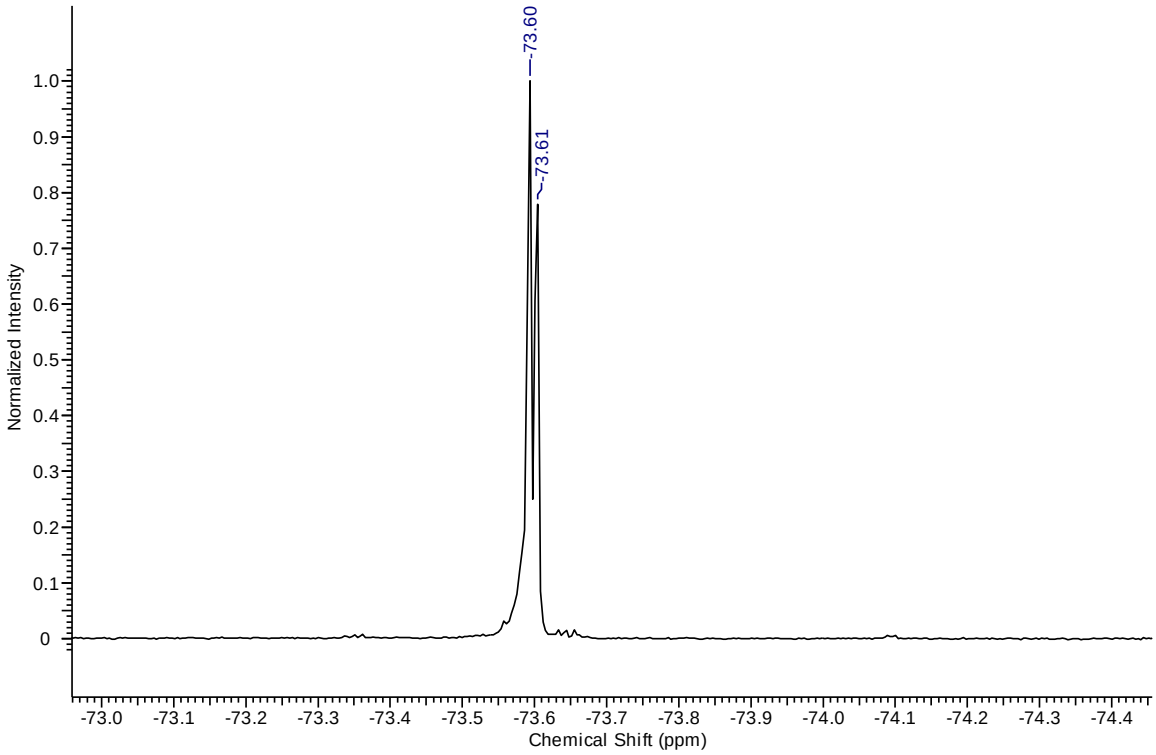

*Figure S49: ^{19}F-NMR (376.5 MHz, chloroform-d, 25°C) spectrum of compound **3**.*

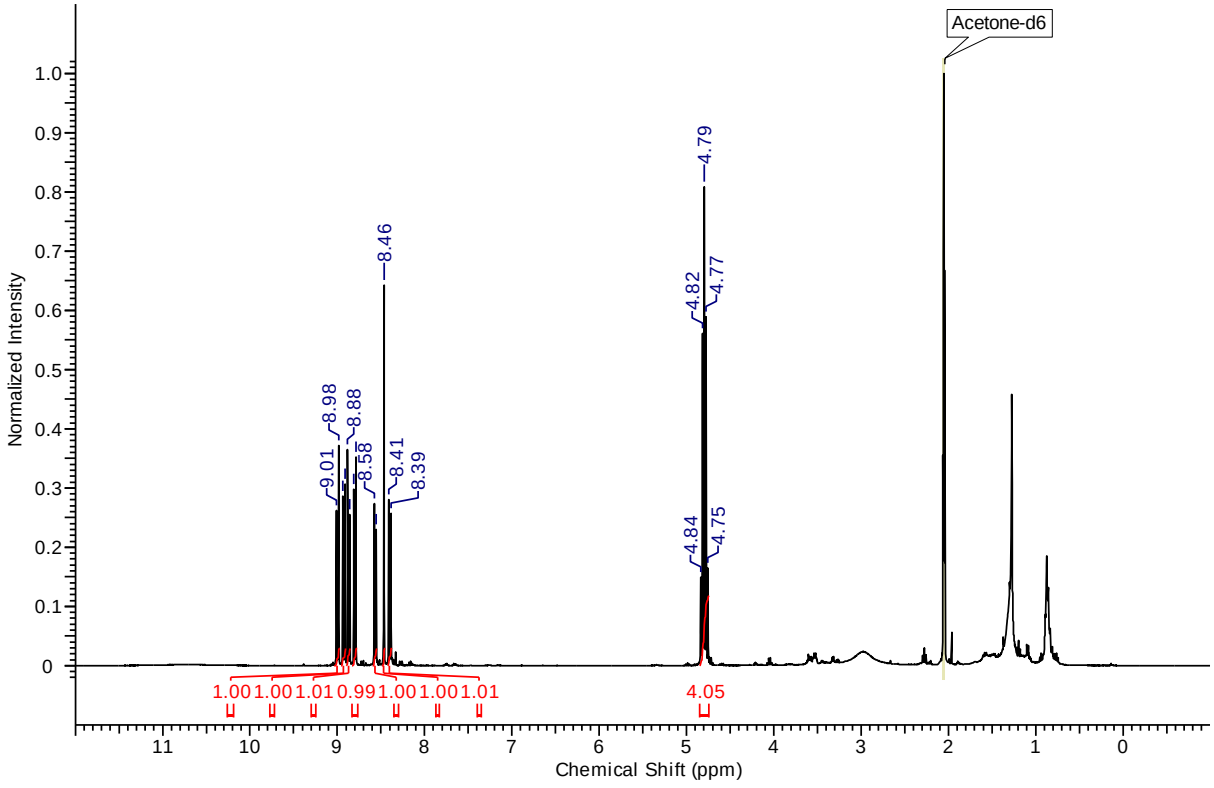

*Figure S50: ^{1}H-NMR (400.13 MHz, acetone-d_6, 25°C) spectrum of compound **4**.*

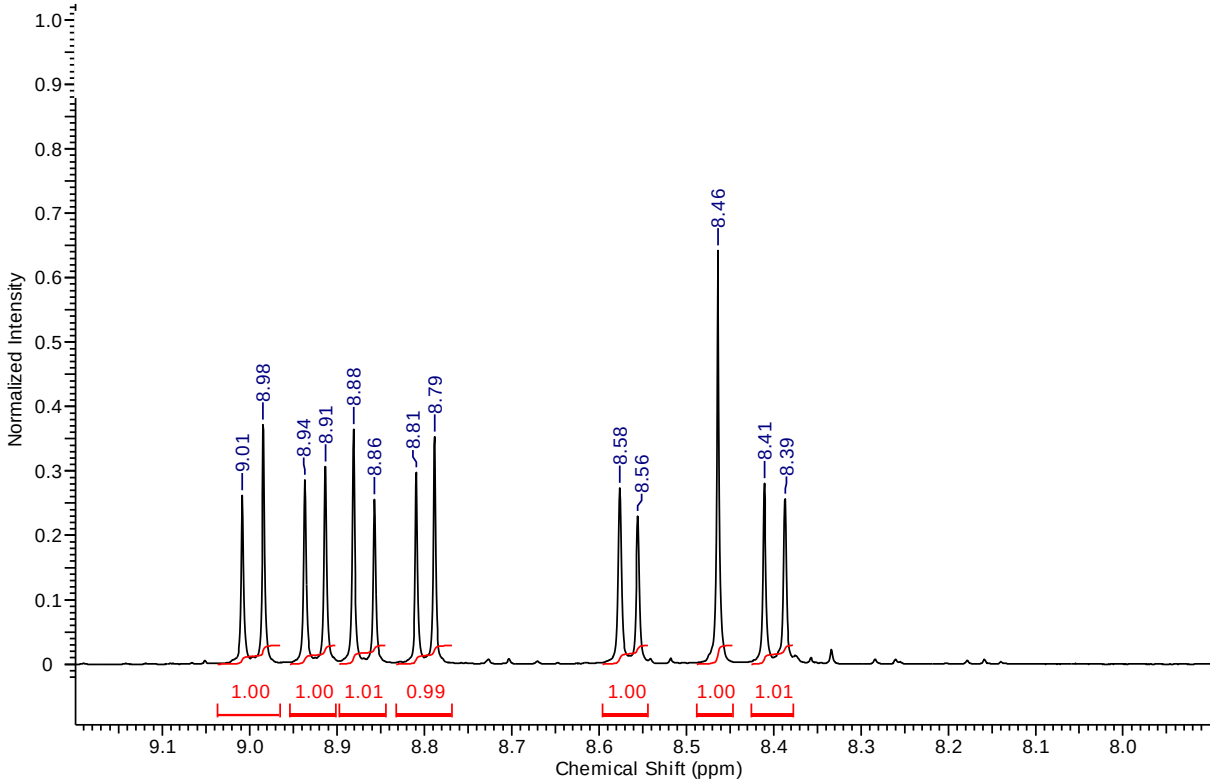

*Figure S51: ^{1}H-NMR (400.13 MHz, acetone-d_6, 25°C) spectrum of compound **4** (zone 1).*

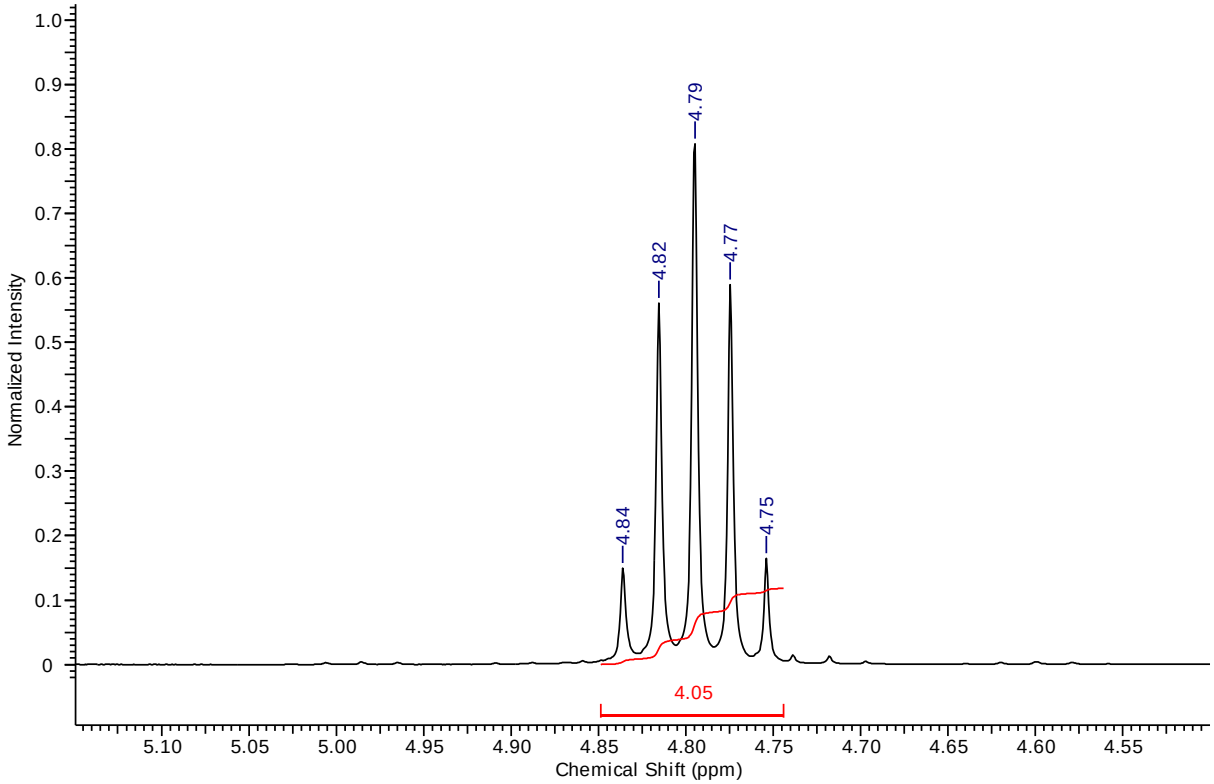

*Figure S52: ^{1}H-NMR (400.13 MHz, acetone-d_6, 25°C) spectrum of compound **4** (zone 2).*

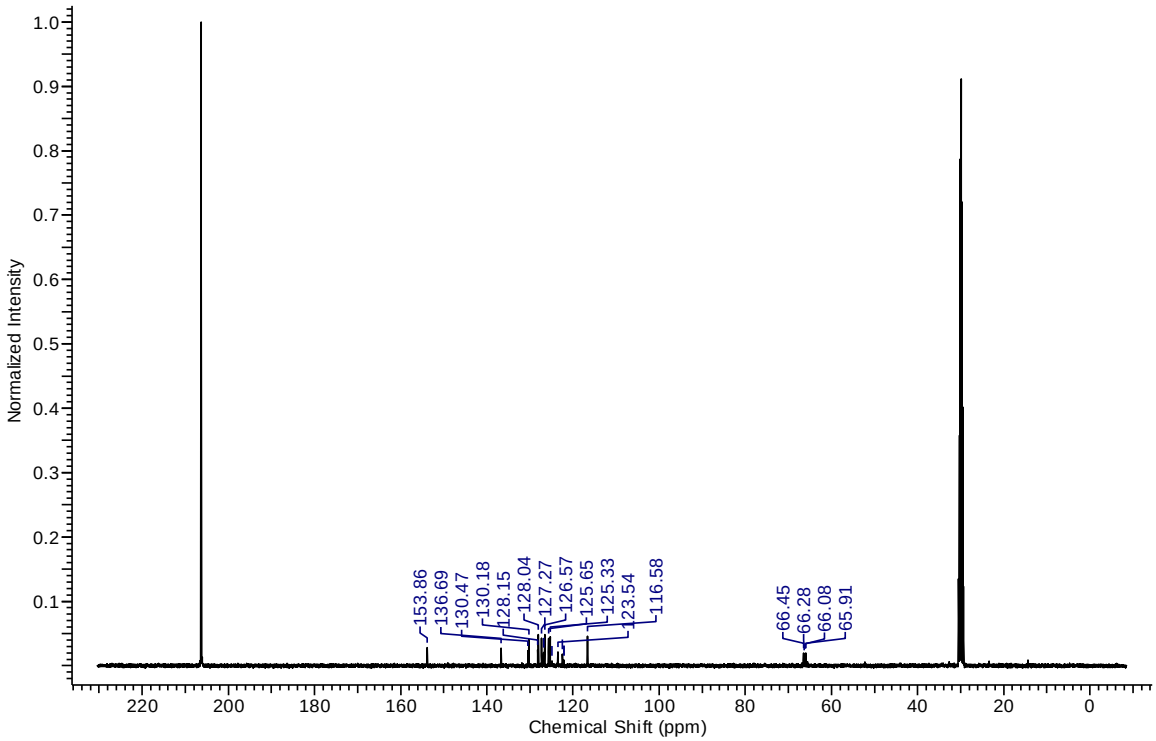

*Figure S53: ^{13}C-NMR (100.61 MHz, acetone-d_6, 25°C) spectrum of compound **4**.*

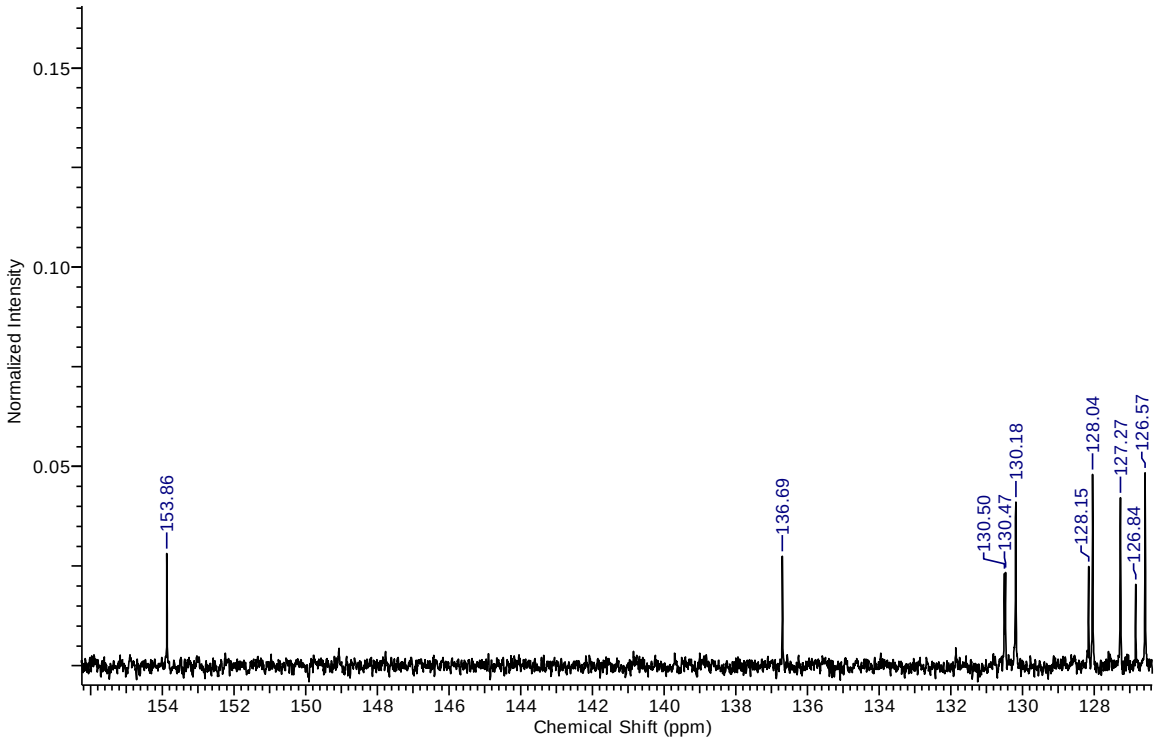

*Figure S54: ^{13}C-NMR (100.61 MHz, acetone-d_6, 25°C) spectrum of compound **4** (zone 1).*

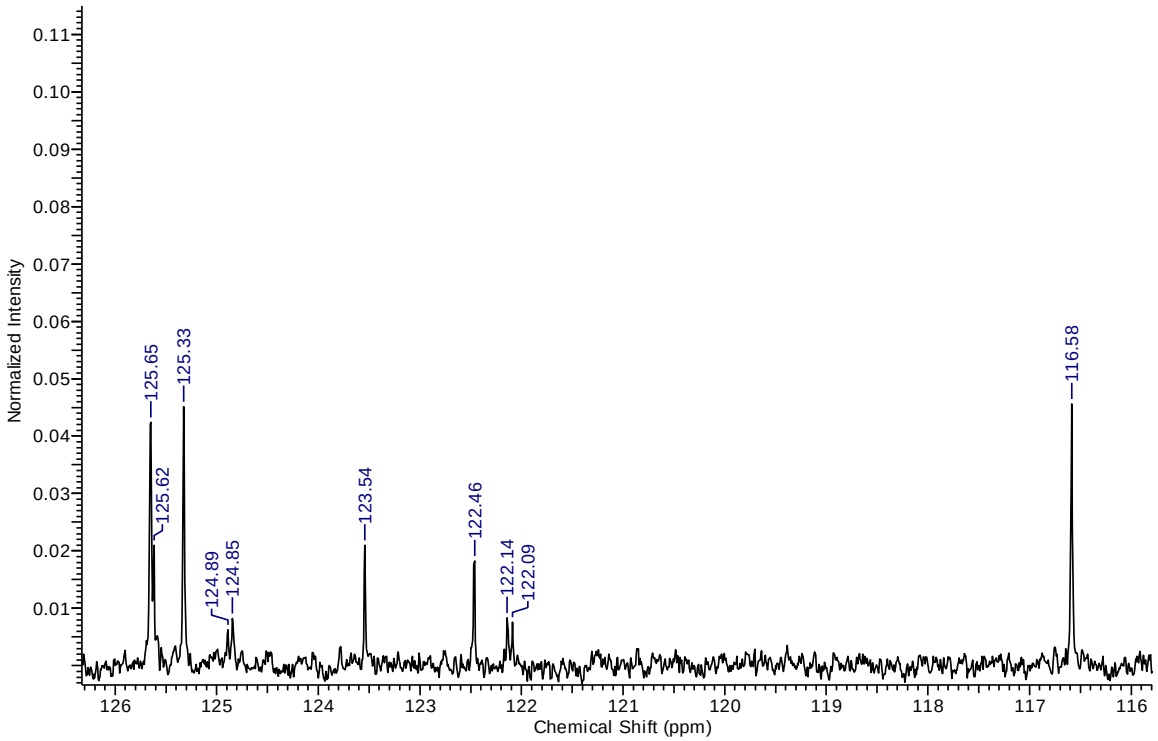

*Figure S55: ^{13}C-NMR (100.61 MHz, acetone-d_6, 25°C) spectrum of compound **4** (zone 2).*

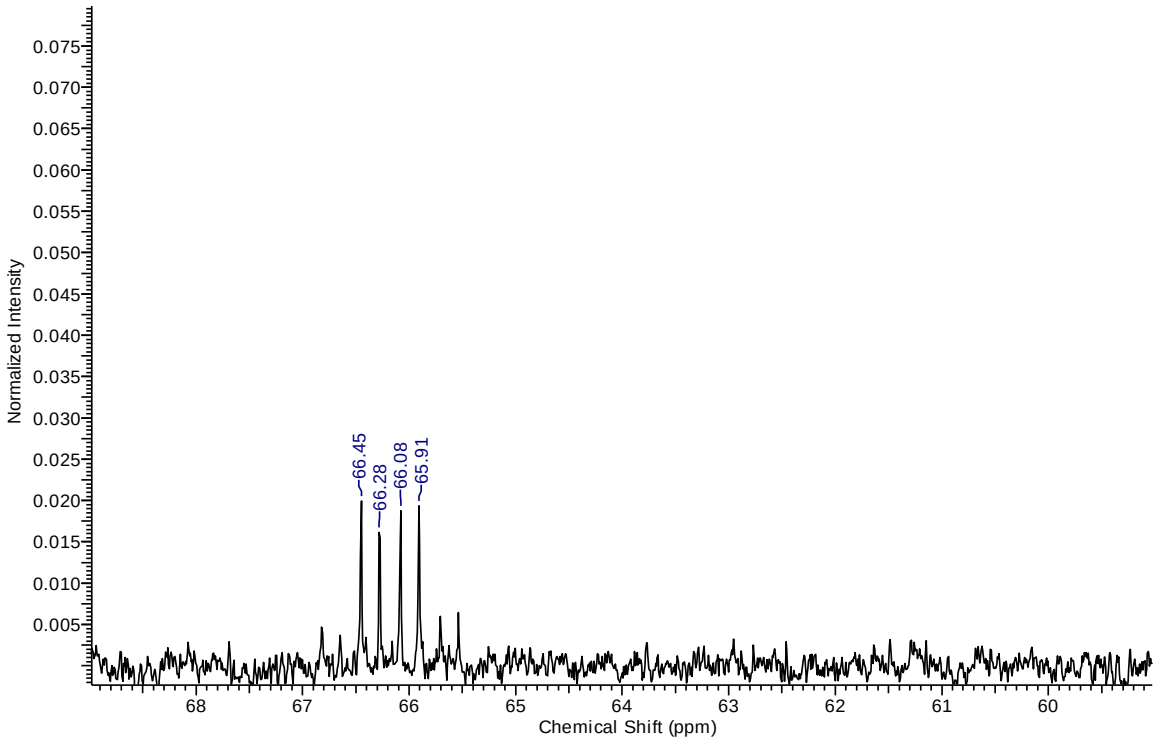

*Figure S56: ^{13}C-NMR (100.61 MHz, acetone-d_6, 25°C) spectrum of compound **4** (zone 3).*

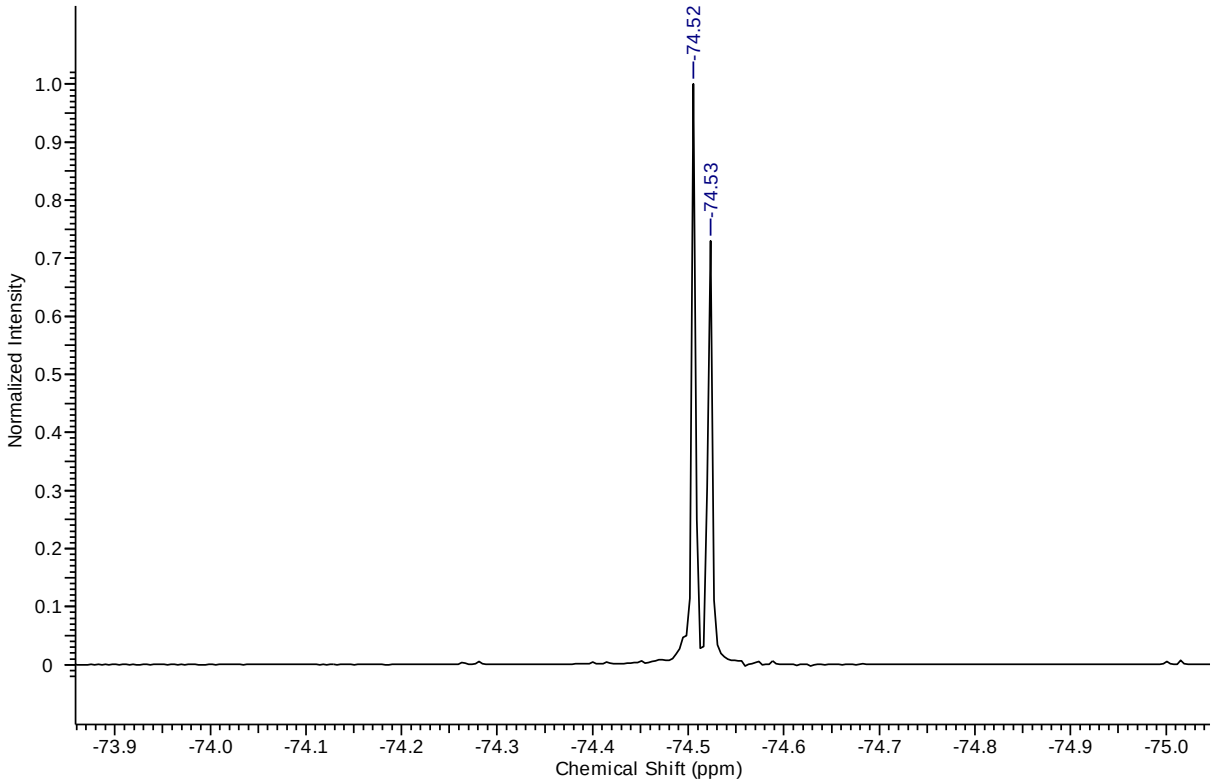

*Figure S57: ^{19}F-NMR (376.5 MHz, acetone-d_6, 25°C) spectrum of compound **4**.*

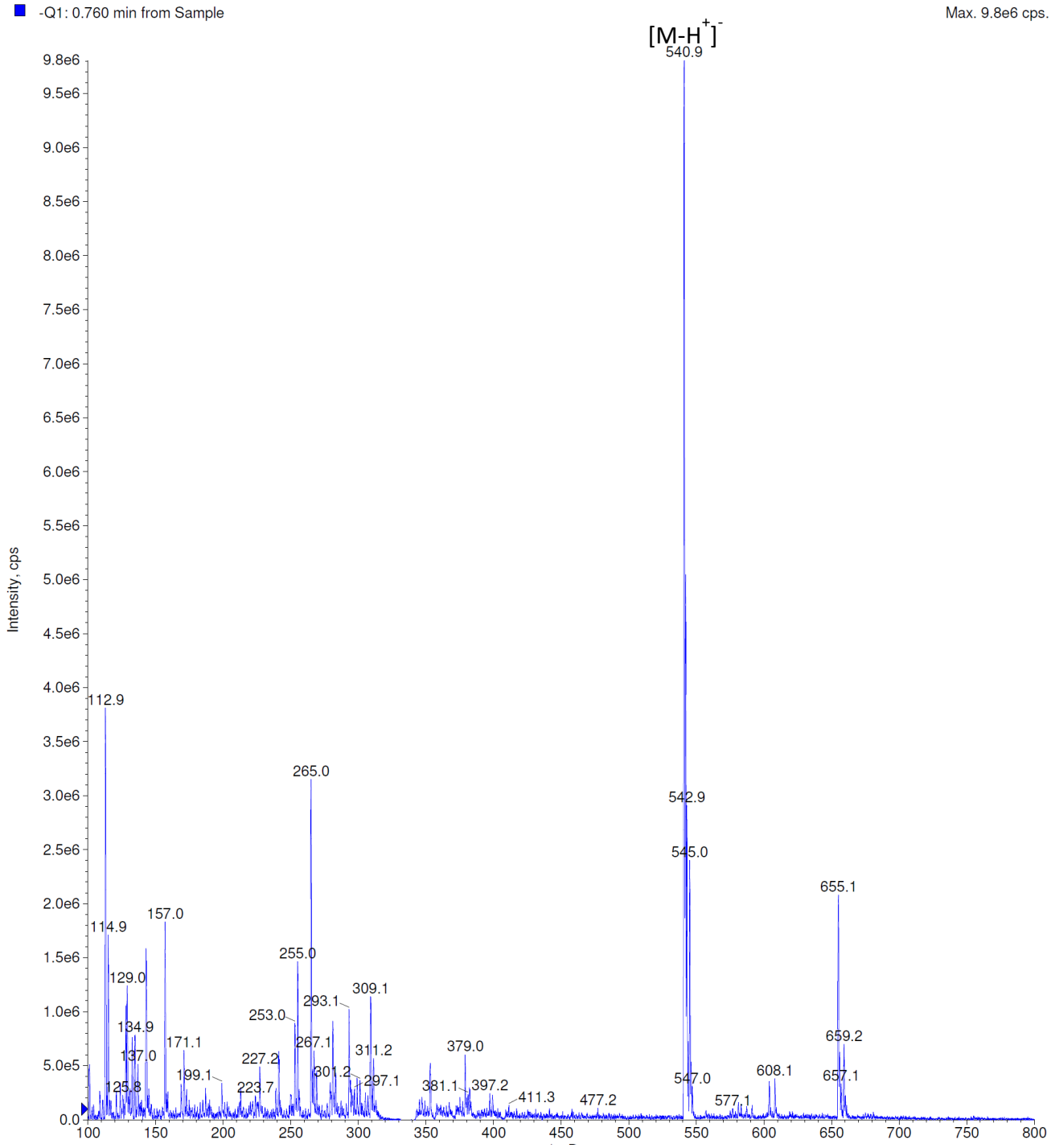

*Figure S58: Mass spectrum (ESI, negative ion mode) of **4**.*

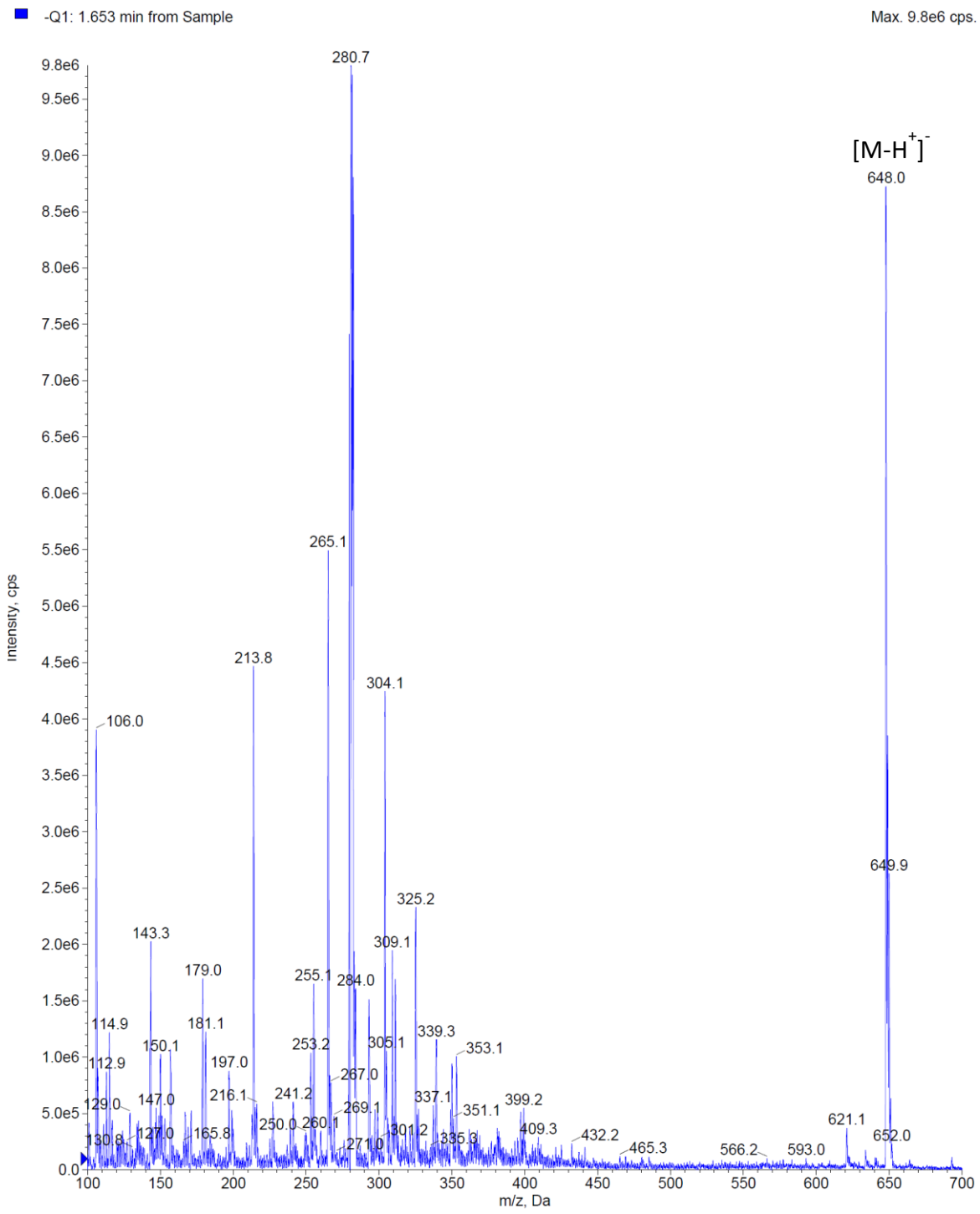

*Figure S59: Mass spectrum (ESI, negative ion mode) of **5b**.*

18. X-ray crystallographic analysis

18.1 Compound 2

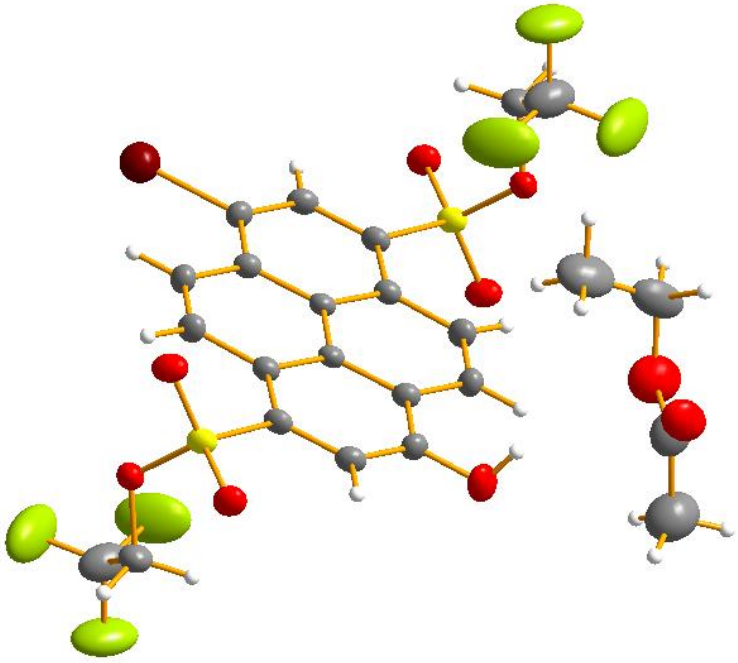

*Figure S60: Crystal structure of compound **2**.*

*Table S9: Crystal data and structure refinement for **2***

Identification code	sh3785	
Empirical formula	C20 H11 Br F6 O7 S2 x C4 H8 O2	
Formula weight	709.42	
Temperature	152(2) K	
Wavelength	0.71073 Å	
Crystal system	Triclinic	
Space group	P-1	
Unit cell dimensions	a = 5.3792(7) Å	α = 108.397(6)°.
	b = 10.8315(14) Å	β = 97.733(6)°.
	c = 13.1574(17) Å	γ = 98.586(6)°.
Volume	705.67(16) $Å^3$	
Z	1	
Density (calculated)	1.669 Mg m^{-3}	
Absorption coefficient	1.694 mm^{-1}	
F(000)	356	
Crystal size	0.406 x 0.147 x 0.030 mm^3	
Theta range for data collection	1.663 to 27.543°.	
Index ranges	-6<=h<=6, -14<=k<=12, -16<=l<=17	
Reflections collected	12193	
Independent reflections	3213 [R(int) = 0.0305]	
Completeness to theta = 25.242°	99.6 %	
Absorption correction	Semi-empirical from equivalents	
Max. and min. transmission	0.7456 and 0.6698	
Refinement method	Full-matrix least-squares on F^2	
Data / restraints / parameters	3213 / 30 / 229	
Goodness-of-fit on F^2	1.055	
Final R indices [I>2sigma(I)]	R1 = 0.0532, wR2 = 0.1476	
R indices (all data)	R1 = 0.0699, wR2 = 0.1608	
Extinction coefficient	n/a	
Largest diff. peak and hole	1.040 and -0.637 e.$Å^{-3}$	

18.2 Compound 3

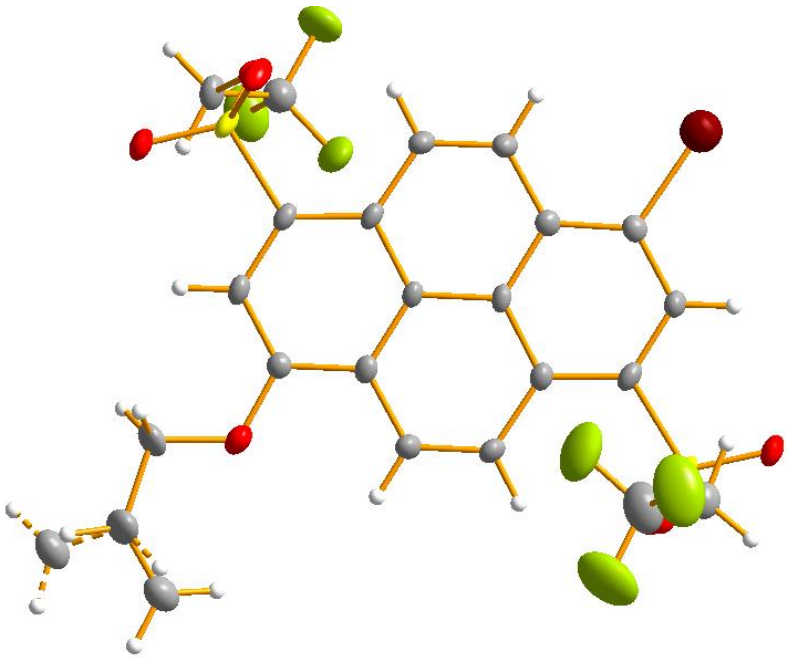

*Figure S61: Crystal structure of compound **3**.*

*Table S8: Crystal data and structure refinement for **3** (sh3982)*

Identification code	sh3982	
Empirical formula	C23 H15 Br F6 O7 S2	
Formula weight	661.38	
Temperature	142(2) K	
Wavelength	0.71073 Å	
Crystal system	Triclinic	
Space group	P-1	
Unit cell dimensions	a = 5.4124(3) Å	α = 87.330(4)°.
	b = 13.1343(7) Å	β = 87.521(4)°.
	c = 17.3655(10) Å	γ = 83.123(4)°.
Volume	1223.38(12) $Å^3$	
Z	2	
Density (calculated)	1.795 Mg m^{-3}	
Absorption coefficient	1.941 mm^{-1}	
F(000)	660	
Crystal size	0.241 x 0.066 x 0.049 mm^3	
Theta range for data collection	1.175 to 28.019°.	
Index ranges	-7<=h<=7, -17<=k<=17, -22<=l<=22	
Reflections collected	22922	
Independent reflections	5875 [R(int) = 0.0566]	
Completeness to theta = 25.242°	99.8 %	
Absorption correction	Semi-empirical from equivalents	
Max. and min. transmission	0.8621 and 0.7768	
Refinement method	Full-matrix least-squares on F^2	
Data / restraints / parameters	5875 / 8 / 362	
Goodness-of-fit on F^2	1.049	
Final R indices [I>2sigma(I)]	R1 = 0.0488, wR2 = 0.1156	
R indices (all data)	R1 = 0.0772, wR2 = 0.1279	
Extinction coefficient	n/a	
Largest diff. peak and hole	1.810 and -0.647 e.$Å^{-3}$	

19. References

[S1] G. M. Sheldrick, *Acta Cryst*. **2008**, A64, 112-122.

[S2] B. Finkler, I. Riemann, M. Vester, A. Grüter, F. Stracke, G. Jung, *Photochem. Photobiol. Sci*. **2016**, 15, 1544-1557.

[S3] S. Schmidt, I. Tavernaro, C. Cavelius, E. Weber, A, Kümper, C. Schmitz, J. Fleddermann, A. Kraegeloh, *Nanoscale Res. Lett*. **2017**, 12, 545.

[S4] D. Maus, A. Grandjean, G. Jung, *J. Chem. Phys*. *A* **2018**, 122, 9025-9030.

[S5] J. R. Lakowicz, *Principles of Fluorescence Spectroscopy,* 4th Edition, Springer, New York, USA **2010**.

[S6] K. Suhling, J. Siegel, D. Phillips, P. M. W. French, S. Lévêque-Fort, S. E. D. Webb, D. M. Davis, *Biophys. J.* **2002**, 83, 3589-3595.

[S7] B. Hinkeldey, A. Schmitt, G. Jung, *ChemPhysChem.* **2008**, 9, 2019-2027.

[S8] B. Finkler, C. Spies, M. Vester, F. Walte, K. Omlor, I. Riemann, M. l. Zimmer, F. Stracke, M. Gerhards, G. Jung, *Photochem. Photobiol. Sci.* **2014**, 13, 548.

[S9] S. J. Strickler, A. Berg, *J. Chem. Phys*. **1962**, 27, 814-822.

[S10] D. M. Jameson, J. C. Croney, *Comb. Chem. High Throughput Screen* **2003**, 6, 167-176.

[S11] B. Hötzer, R. Ivanov, S. Altmeier, R. Kappl, G. Jung, *J. Fluoresc.* **2011**, 21, 2143-2153.

[S12] P. Wahl, G. Weber, *J. Mol. Biol.* **1967**, 30, 371-382.

[S13] D. M. Jameson, J. A. Ross, *Chem. Rev.* **2010**, 110, 2685-2708.